1 **Size distribution and coating thickness of black carbon from the Canadian oil sands operations**

2 Yuan Cheng[1], Shao-Meng Li[1,*], Mark Gordon[2], Peter Liu[1]

3 [1] Air Quality Research Division, Environment and Climate Change Canada, 4905 Dufferin Street,
4 Toronto, Ontario M3H 5T4, Canada

5 [2] Department of Earth and Space Science and Engineering, York University, 4700 Keele Street,
6 Toronto, Ontario M3J 1P3, Canada

7 * Corresponding author: shao-meng.li@canada.ca

8 **Abstract**

9 Black carbon (BC) plays an important role in the Earth's climate system. However, parameterizations

10 of BC size and mixing state have not been well addressed in aerosol-climate models, introducing

11 substantial uncertainties into the estimation of radiative forcing by BC. In this study, we focused on

12 BC emissions from the oil sands (OS) surface mining activities in northern Alberta, based on an

13 aircraft campaign conducted over the Athabasca OS region in 2013. A total of 14 flights were made

14 over the OS source area, in which the aircraft was typically flown in a 4- or 5-sided polygon pattern

15 along flight tracks encircling an OS facility. Another 3 flights were performed downwind of the OS

16 source area, each of which involved at least three intercepting locations where the well-mixed OS

17 plume was measured along flight tracks perpendicular to the wind direction. Comparable size

18 distributions were observed for refractory black carbon (rBC) over and downwind of the OS facilities,

19 with rBC mass median diameters (MMD) between ~ 135 and 145 nm that were characteristic of fresh

20 urban emissions. This MMD range corresponded to rBC number median diameters (NMD) of ~ 60−70

21 nm, approximately 100% higher than the NMD settings in some aerosol-climate models. The typical

22 in- and out-of-plume segments of a flight, which had different rBC concentrations and photochemical

23 ages, showed consistent rBC size distributions in terms of MMD, NMD and the corresponding

24 distribution widths. Moreover, rBC size distributions remained unchanged at different downwind

25 distances from the source area, suggesting that atmospheric aging would not necessarily change rBC

26 size distribution. However, aging indeed influenced rBC mixing state. Coating thickness for rBC cores

27 in the diameter range of 130−160 nm was nearly doubled (from ~ 20 to 40 nm) within three hours

28 when the OS plume was transported over a distance of 90 km from the source area.

1. Introduction

Oil sands (OS), a type of unconventional petroleum deposit, are naturally occurring mixtures of bitumen (a viscous form of crude oil), sand, water, and small amounts of other contaminants. The OS deposit in Alberta, Canada, is estimated to contain about 1.7 trillion barrels of bitumen. This deposit is distributed in the Athabasca, Cold Lake and Peace River regions, covering a total area of ~ 1.42×10^5 km^2, of which about 10% can be recovered economically with existing technologies (Government of Alberta, 2009). Bitumen can be recovered in two ways, i.e., surface mining for the shallow reserves (e.g., less than 75 m below the surface) and using in situ technologies for the deeper deposits. Surface mining can be applied to an area of only 4800 km^2 area within the Athabasca region; and by 2013, about 19% of this surface minable area had been disturbed (Alberta Energy, 2017). As demand for crude oil fluctuated, oil production from the Alberta oil sands experienced periods of rapid expansion and stabilized production over the last decade, with total OS production doubling between 2004 (1.1 million barrels per day, with about 66% from surface mining) and 2014 (2.2 million barrels per day, with about 47% from surface mining) (Alberta Energy, 2016).

The OS industry in Alberta has raised concerns on environmental impacts. For example, measurement results from Kelly et al. (2009, 2010) and Kurek et al. (2013) showed that the OS development contributed organic (e.g., polycyclic aromatic hydrocarbons, PAHs) and inorganic (e.g., mercury, nickel, and thallium) pollutants to the Athabasca River watershed; model simulations by Parajulee and Wania (2014) indicated that the Canadian National Pollutant Release Inventory (NPRI) likely underestimated PAHs emissions in the Athabasca OS region. Despite these studies, both the emissions and subsequent environmental impacts remain poorly understood for pollutants from the Alberta OS industry. To help address this lack of understanding, an aircraft campaign was conducted with measurements of an extensive set of air pollutants over the Athabasca OS region in the summer of 2013. Using results from the campaign, Shephard et al. (2015) validated profiles of ammonia, carbon monoxide, formic acid, and methanol retrieved from the Tropospheric Emission Spectrometer (TES) satellite; Liggio et al. (2016, 2017) demonstrated the large OS surface mining facilities in Athabasca as a significant source of secondary organic aerosol (SOA) and gaseous organic acids; and

56 Li et al. (2017) identified the surface mining facilities as a greater source of volatile organic

57 compounds (VOCs) than previously realized.

58 In addition to gaseous pollutants and SOA, another focus of the 2013 aircraft campaign was

59 black carbon (BC) emissions from the surface mining facilities and its transport downwind. BC is a

60 distinct type of carbonaceous material formed during incomplete combustion of fossil and biomass

61 fuels, which is strongly light-absorbing in the visible light spectral range, refractory, insoluble and

62 typically appears as chain-like aggregates consisting of fewer than 10 to several hundred carbon

63 spherules (Andreae and Gelencsér, 2006; Bond et al., 2013; Petzold et al., 2013; Buseck et al., 2014).

64 BC plays a unique and important role in the Earth's climate system as an effective absorber of solar

65 radiation. It has relatively short atmospheric residence times but can exert a strong warming effect on

66 global and regional climate (Ramanathan and Carmichael, 2008; Bond et al., 2013; Myhre et al.,

67 2013). Therefore, BC emission reduction has long been considered as an important near-term climate

68 mitigation target. However, each step along the way between source and environmental effect of BC is

69 complex. For example, anthropogenic BC emissions and the resulting temporal and spatial variations

70 of BC, which can be simulated by chemical transport models, remain highly uncertain (Samset et al.,

71 2014); parameterizations of BC size and mixing state have not been well addressed in state-of-the-art

72 radiative transfer models (Morgenstern et al., 2017). Both factors are recognized as important sources

73 of uncertainties in the estimate of climate forcing by BC (IPCC, 2013).

74 For large-scale industrial activities such as the OS surface mining operations in Athabasca, key

75 concerns regarding BC include (but are not limited to) the quantities of BC emitted into the

76 atmosphere, size distribution and mixing state of the freshly emitted BC particles, evolution of the BC

77 particles including their size, mixing state and optical properties as the OS plumes are transported

78 downwind, and BC deposition. In this study, a total of 17 flights conducted during the 2013 aircraft

79 campaign were investigated to characterize BC emissions from six major OS surface mining facilities

80 in the Athabasca region, with focuses on the evolution of BC size distribution and mixing state.

81 Airborne BC measurements were performed by a Single Particle Soot Photometer (SP2). BC mass and

82 number size distributions were determined and compared not only for different facilities but also for

83 different downwind distances. BC mixing state was estimated by coating thickness retrieved from the

84 SP2, based on which the influences of photochemical aging were illustrated. Limitations of using this

85 coating thickness to represent BC mixing state were also discussed. These results can provide insights

86 into the evolution of BC aerosol in the real atmosphere.

87 **2. Methods**

88 **2.1 Aircraft campaign**

89 The aircraft campaign was conducted over the Athabasca OS region in northern Alberta between

90 August 13 and September 7, 2013 in support of the Joint Canada-Alberta Implementation Plan for Oil

91 Sands Monitoring (JOSM). Using instruments installed aboard the National Research Council Institute

92 for Aerospace Research Convair-580 research aircraft, an extensive set of air pollutants (including

93 both gaseous and particulate species) were determined with high time resolutions (Gordon et al., 2015;

94 Liggio et al., 2016; Li et al., 2017). During this campaign, 22 flights were made for a total of about 84

95 hours, without influences of wet removal and cloud processing. These flights were designed (1) to

96 quantify emissions of air pollutants from six major OS surface mining facilities including Syncrude

97 Mildred Lake (SML), Suncor Energy OSG (SUN), Canadian Natural Resources Limited Horizon

98 (CNRL), Shell Albian and Jackpine (SAJ), Syncrude Aurora (SAU), and Imperial Kearl Oil Sands

99 Mine (IKL), and (2) to determine atmospheric evolution of the primary pollutants. The details of the

100 measurements, the flight patterns, and objectives of the flights were described in detail by Liggio et al.

101 (2016) and Li et al. (2017). In 14 flights for emission quantitation, the aircraft was typically flown in

102 a 4- or 5-sided polygon pattern encircling an OS surface mining facility, with level flight tracks at

103 8−10 altitudes increasing from 150 to 1370 m above ground and reaching above the mixed layer; these

104 level flight tracks were stacked along the sides of the polygon to form a virtual box encasing the

105 facility (Figures 1a and S1a). Repeated emission flights were made over SML, SUN, CNRL, and SAJ,

106 whereas single flights were made over SAU and IKL.

107 Three flights were designed to study transformation of air pollutants emitted from the OS surface

108 mining facilities. They were conducted in a Lagrangian pattern such that the same OS plume was

109 sampled at different time intervals (approximately 1 hour apart) as it was transported downwind from

4

110   the source area (Figures 1b and S1b). Real-time wind speed and direction measurements were used to

111   guide the intercepting locations. The first intercepting locations were chosen at about 1 hour

112   downwind of the majority of the OS facilities so that the emitted air pollutants were well mixed and

113   merged into large plumes. At each intercepting position, the aircraft was flown along level flight

114   tracks perpendicular to the wind direction at multiple altitudes; then these level flight tracks were

115   stacked vertically to create a virtual screen downwind of the OS source area. At least three screens

116   were created for each transformation flight, without industrial emissions in between.

117   **2.2 Aerosol Sampling**

118   Aerosols were sampled through an isokinetic, shrouded solid diffuser inlet (Droplet Measurement

119   Technologies Inc., Boulder, CO, USA) with a NASA design as described in Huebert et al. (2004). The

120   inlet was shared by all aerosol instruments inboard the aircraft, including a High-Resolution Time-of-

121   Flight Aerosol Mass Spectrometer (HR-ToF-AMS; Aerodyne Research Inc., Billerica, MA, USA), a

122   Condensation Particle Counter (CPC, Model 3775; TSI Inc., Shoreview, MN, USA), an Ultra-High

123   Sensitivity Aerosol Spectrometer and a Single Particle Soot Photometer (UHSAS and SP2; Droplet

124   Measurement Technologies Inc., Boulder, CO, USA). The UHSAS measures particle number size

125   distribution in the 0.06 to 1.0 μm diameter range. Aerosol number size distributions were also

126   measured using a Forward Scattering Spectrometer Probe (FSSP, Model 300; Particle Measuring

127   Systems Inc., Boulder, CO, USA) housed in a pod and mounted under the right wing of the aircraft.

128   The FSSP has a non-intrusive inlet-less design and measures particle number size distribution in the

129   0.3 to 20 μm diameter range. A comparison of the measurement results from the UHSAS and FSSP in

130   the overlapping size range of 0.3 to 1.0 μm showed an agreement in terms of both particle numbers

131   and their size distributions (Figure S2). This comparison suggests that in the inlet and sampling line,

132   both the particle loss and the evaporation loss from the particles were minimal for the < 1.0 μm size

133   range.

134   **2.3 BC measurements by the SP2**

135   From the common inlet and sampling line, a SP2 was used to measure the refractory black carbon

136   (rBC) cores on a particle-by-particle basis based on incandescent light emitted from heated rBC cores

137   when they cross and absorb energy from a laser beam (Stephens et al., 2003; Baumgardner et al., 2004;

138   Schwarz et al., 2006; Moteki and Kondo, 2010; Laborde et al., 2012a). The SP2 used in this study

139   detected single particle rBC cores in the mass range of $\sim 0.3-16$ fg, based on the calibration using

140   regal black particles (Cappa et al., 2012). To account for the rBC cores outside this detection range, a

141   lognormal fit was applied to the measured rBC size distribution and then extrapolated over $10-1000$

142   nm (Schwarz et al., 2006). Here the rBC size refers to the mass equivalent diameter (D_{MEV}) calculated

143   as $\left[\left(6\times m\right)/\left(\rho\times\pi\right)\right]^{1/3}$, where m and ρ are the mass and density of the rBC core, respectively. The

144   value of ρ was assumed to be 1.8 g/cm^3, which is the median ρ value recommended by Bond and

145   Bergstrom (2006). Based on this ρ value, the SP2's detection range for single particle rBC core mass

146   ($\sim 0.3-16$ fg) corresponded to an rBC size detection range of $\sim 70-260$ nm in terms of D_{MEV}. For

147   either rBC mass or number concentration, a scaling factor (F_{rBC}) was calculated as $I_{whole}/I_{detected}$, where

148   I_{whole} indicates the integral of the lognormal fitting curve from 10 nm to 1000 nm, and $I_{detected}$ indicates

149   the integral of the curve from 70 nm to 260 nm. Subsequently, the final rBC concentration could be

150   determined as $F_{rBC} \times C_{detected}$, where $C_{detected}$ is the detected rBC concentration (either mass or number)

151   derived from the SP2. All the rBC concentrations involved in this paper have been scaled by flight-

152   specific F_{rBC}.

153   In addition to emitting incandescent radiation, rBC containing particles also scatter light when

154   passing through the laser beam of the SP2. Coating thicknesses on rBC cores ($T_{coating}$, in nm) can be

155   retrieved from the scattering signals on a particle-by-particle basis, using Mie theory calculation with

156   a series of assumptions (Schwarz et al., 2008a, b; Laborde et al., 2012b). To calculate $T_{coating}$ for an

157   rBC containing particle, the internally mixed particle needs to be idealized as a two-component sphere

158   with a concentric core-shell morphology. In this study, the rBC core was assumed to have a complex

159   refractive index of $2.26 - 1.26i$, which was initially suggested by Moteki et al. (2010) and

160   subsequently confirmed by Taylor et al. (2015). The coating material on a rBC core was assumed to

161   have a complex refractive index of $1.5 - 0i$, which is representative of the corresponding values

162   determined for inorganic salts (e.g., ammonium sulfate) and secondary organic aerosol (Schnaiter et

163 al., 2005; Lambe et al., 2013). The core size was held fixed at D_{MEV} of the rBC core, whereas the

164 diameter of the whole particle was varied in the Mie calculation until the modeled scattering cross

165 section matched the measurement. Measured scattering cross section was determined by a leading-

166 edge-only (LEO) fit to the recorded scattering signal (Gao et al., 2007). Finally, $T_{coating}$ was calculated

167 as the difference between the radii of the whole particle and the rBC core.

168   A key step to retrieve $T_{coating}$ of an rBC containing particle from its scattering signal (S) is the

169 LEO fit, which requires, at least, S can be properly measured (Schwarz et al., 2008a, b; Laborde et al.,

170 2012b; Liu et al., 2014). The LEO fit cannot be performed when S is outside the SP2's detection range

171 of scattering intensity. Thus, $T_{coating}$ cannot be calculated for relatively small rBC cores with thin

172 coatings (i.e., rBC containing particles with S below the lower detection limit of scattering intensity)

173 or relatively large rBC cores with thick coatings (i.e., rBC containing particles with S above the upper

174 detection limit of scattering intensity) (Metcalf et al., 2012; Dahlkötter et al., 2014). This limitation

175 prohibits a direct comparison of $T_{coating}$ across all rBC cores with different sizes.

176   Moreover, the retrieved $T_{coating}$ could be considerably influenced by uncertainties introduced by

177 the LEO fit. These uncertainties can be evaluated using non-rBC containing particles. The scattering

178 signals of non-rBC containing particles always have the shape of a full Gaussian curve, since they will

179 not evaporate or change in size when passing through the SP2's laser beam. Thus, for non-rBC

180 containing particles, the LEO fit should in principle lead to the same scattering amplitude or the same

181 optical size ($D_{optical}$) as that retrieved from a fit to the full scattering signal (i.e., the full-Gaussian fit)

182 (Gao et al., 2007). In this study, the LEO and full-Gaussian fits agreed within approximately ± 15% in

183 determining $D_{optical}$ for non-rBC containing particles (Figure 2). Here $D_{optical}$ were calculated from the

184 fitted scattering amplitudes, by assuming a complex refractive index of $1.5 - 0i$ for non-rBC

185 containing particles. $D_{optical}$ was used in Figure 2 to evaluate the agreement between the LEO and full-

186 Gaussian fits because it was more directly related to $T_{coating}$ compared to the scattering amplitude.

187 **2.4 Additional data set used**

188   Organic aerosol (OA) mass was measured with a time resolution of 10 s by the HR-ToF-AMS.

189 Photochemical age was calculated as $-\log_{10}(NO_x/NO_y)$, where NO_x is the sum of nitrogen monoxide

7

190 and nitrogen dioxide (i.e., NO + NO$_2$) and NO$_y$ refers to the total reactive oxidized nitrogen

191 compounds (Kleinman et al., 2008). Measurements of OA, NO$_x$ and NO$_y$ during the aircraft campaign

192 have been described elsewhere (Liggio et al., 2016).

193 **3. Results and Discussion**

194 **3.1 rBC size distributions over the OS source region: facility-integrated results**

195   For each flight, the measured masses of the individual rBC cores over the entire flight were first

196 grouped into different size bins and then fitted by a lognormal curve:

197
$$\frac{\mathrm{d}m}{\mathrm{d}\log D_{\mathrm{MEV}}} = A_{\mathrm{mass}} \times \exp\left\{0 - \left[\frac{\ln\left(D_{\mathrm{MEV}}/X_{1,\,\mathrm{mass}}\right)}{X_{2,\,\mathrm{mass}}}\right]^2\right\} \tag{1}$$

198 where A_{mass}, $X_{1,\,\mathrm{mass}}$ and $X_{2,\,\mathrm{mass}}$ are the fitting parameters. The fitting parameter $X_{1,\,\mathrm{mass}}$ will be termed

199 the mass median diameter (MMD), and the fitting parameter $X_{2,\,\mathrm{mass}}$ will be loosely referred to as the

200 mass distribution width (Width$_{\mathrm{mass}}$) which can be converted to the standard deviation of the

201 distribution (σ_{mass}) by $\sigma_{\mathrm{mass}} = \exp\left(\mathrm{Width}_{\mathrm{mass}}/\sqrt{2}\right)$. As can be seen from Equation (1), A_{mass} is

202 proportional to the absolute value of rBC mass concentration and thus it is unimportant for describing

203 the shape of a lognormal curve. This is particularly the case for comparison of rBC size distributions

204 among different OS facilities. It should also be noted that the mass-based scaling factor ($F_{\mathrm{rBC,\,mass}}$),

205 which accounts for the rBC masses outside the SP2's detection range, is independent of A_{mass}.

206 Therefore, A_{mass} will not be further discussed in rBC size distribution. Similarly, rBC number-size

207 distribution could be expressed as:

208
$$\frac{\mathrm{d}N}{\mathrm{d}\log D_{\mathrm{MEV}}} = A_{\mathrm{number}} \times \exp\left\{0 - \left[\frac{\ln\left(D_{\mathrm{MEV}}/X_{1,\,\mathrm{number}}\right)}{X_{2,\,\mathrm{number}}}\right]^2\right\} \tag{2}$$

209 where A_{number}, $X_{1,\,\mathrm{number}}$ and $X_{2,\,\mathrm{number}}$ are the fitting parameters. $X_{1,\,\mathrm{number}}$ and $X_{2,\,\mathrm{number}}$ will be termed

210 the number median diameter (NMD) and the number distribution width (Width$_{\mathrm{number}}$), respectively.

211 Width$_{\mathrm{number}}$ can be converted to the standard deviation of the rBC number-size distribution (σ_{number}) by

212 $\sigma_{\mathrm{number}} = \exp\left(\mathrm{Width}_{\mathrm{number}}/\sqrt{2}\right)$.

213   Mass and number size distributions of rBC are summarized in Figure 3 for the 14 emission

214   flights. As shown in Figure 3, the rBC MMD and NMD were typically in the range of 135−145 nm

215   and 60−70 nm, respectively, while both the mass and number distribution widths were approximately

216   0.7 (the corresponding σ_{mass} and σ_{number} were about 1.6). Most of the rBC from the surface mining

217   facilities were from the heavy diesel trucks used to transport the mined oil sands ores to centralized

218   locations in each facility for bitumen separation from the sands. In most cases, rBC emissions from

219   the six major OS surface mining facilities exhibited similar size distributions. These rBC size

220   distributions are comparable with those observed for urban emissions and source (or near-source)

221   samples representing different types of engine exhausts (Table 1). For example, (1) during an airborne

222   measurement conducted as part of the CalNex 2010 campaign, rBC MMD was estimated to be 122 nm

223   over the Los Angeles Basin (Metcalf, et al., 2012); (2) rBC MMD observed in urban outflows were

224   typically in the range of 140−180 nm, as evidenced by ground-based measurement downwind of

225   Tokyo (Shiraiwa et al., 2007), and by aircraft-based observations over Texas (Schwarz et al., 2008a),

226   California (Sahu et al., 2012) and western and northern Europe (McMeeking et al., 2010); (3) when

227   mainly impacted by traffic emissions, rBC MMD were about 100 and 120 nm for a suburban site in

228   Paris (Laborde et al., 2013) and an urban site in London (Liu et al., 2014), respectively; (4) rBC MMD

229   measured at urban sites in Tokyo, Japan (Kondo et al., 2011b) and Sacramento, CA (Cappa et al.,

230   2012) were between 140 and 150 nm; (5) a laboratory study showed that the MMD was about 125 nm

231   for rBC cores emitted from a diesel car (Laborde et al., 2012b); (6) a MMD of 126 nm was observed

232   for rBC at the Cranfield airport in UK, attributable to aircraft engine exhausts (McMeeking et al.,

233   2010). Although not all of these studies determined rBC MMD and NMD simultaneously, rBC NMD

234   were typically in the range of ~ 60 to 80 nm for urban emissions dominated by contributions from

235   fossil fuel combustion (e.g., Schwarz et al., 2008a; Kondo et al., 2011b; Metcalf, et al., 2012).

236   A comparison of rBC size distributions between this study and previous ones confirms the

237   finding that rBC cores emitted from fossil fuel combustion were smaller in size compared to those

238   from biomass burning (e.g., Schwarz et al., 2008a). The rBC MMD and NMD measured in biomass

239   burning plumes were typically around 200 and 140 nm (Table 1), respectively, which were supported

240   by airborne measurements over Texas (Schwarz et al., 2008a), California (Sahu et al., 2012), Canada

241   (Kondo et al., 2011a; Taylor et al., 2014) and the Arctic (Kondo et al., 2011a). However, wet

242   deposition could lead to a large decrease (e.g., as much as 50 nm) in the MMD of rBC cores in

243   biomass burning plumes (Taylor et al., 2014), suggesting that an rBC MMD substantially smaller than

244   200 nm does not exclude the possibility of biomass burning contributions.

245   Different assumptions have been made by aerosol-climate models for the size distribution of

246   black carbon. For example, the NMD of black carbon emitted by fossil fuel combustion were assumed

247   to be 30, 40 and 60 nm by Dentener et al. (2006; for AeroCom Phase I models), Heald et al. (2014; for

248   a radiative transfer model coupled with GEOS-Chem) and Stier et al. (2005; for the aerosol-climate

249   modelling system ECHAM5-HAM), respectively. According to the SP2 measurement results on rBC,

250   including results from the present study, a NMD of 60 nm would be a more appropriate input

251   parameter in the models for black carbon emissions from fossil fuel combustion. However, there is

252   also a need to evaluate the unimodal assumption for black carbon size distribution (Liggio et al., 2012;

253   Buffaloe et al., 2014), given the SP2's limited detection range of rBC core size.

254   **3.2 rBC size distributions over the OS source region: time-resolved results**

255   In addition to the facility-integrated results (Figure 3), log-normal fits were also applied to 2-min

256   intervals of rBC data derived from the SP2. Figures 4 and 5 show results from the emission flights

257   conducted for CNRL on August 26, 2013 (i.e., F_8/26) and for SUN on August 28, 2013 (i.e., F_8/28),

258   respectively. In both cases, the rBC mass and number size distributions did not exhibit major temporal

259   variations, despite the minor fluctuations observed during F_8/28. The stable rBC size distribution

260   within a flight can be more readily seen from Figure 6a, which indicates that the rBC MMD, mass

261   distribution width and therefore the mass-based scaling factor ($F_{rBC, mass}$) were independent of rBC

262   concentration. As shown in Figure 6a and Table 2, the variations of rBC MMD, mass distribution

263   width, and $F_{rBC, mass}$ were within 5% for F_8/26. Larger variations in rBC size distribution were

264   observed for F_8/28, but the variations in these three parameters were still within 10%. The variations

265   of rBC NMD, number distribution width, and number-based scaling factor ($F_{rBC, number}$) were also

266   within 10% for both F_8/26 and F_8/28 (Table 2).

267 The temporal variations of rBC concentration shown in Figures 4 and 5 were mainly driven by

268 the in- vs. out-of-plume differences. There was a sharp increase in rBC concentration when the aircraft

269 flew into a plume, whereas the rBC concentration deceased rapidly when the aircraft left the plume.

270 Therefore, the stable rBC size distributions observed for the emission flights, which were clearly

271 independent of rBC concentration (e.g., Figure 6a), mean negligible difference in the rBC size

272 distribution between the in- and out-of-plume conditions over the OS source region. The size

273 distribution consistency for rBC is observed regardless of the threshold rBC concentration used to

274 distinguish the in- and out-of-plume conditions, which is flight-dependent (e.g., $\sim$ 0.1 $\mu g/m^3$ in terms

275 of 2-min averaged rBC mass concentration for F_8/26 as shown in Figure S3). The implications of

276 consistent size distributions for rBC near the sources are further discussed in Section 3.3 together with

277 results from the transformation flights.

278 In addition to rBC concentration, the in- and out-of-plume air masses had different

279 photochemical ages as indicated by their values of $-\log_{10}(NO_x/NO_y)$ determined from concurrent

280 measurements of NO_x and NO_y. As shown in Figure 6b, there was a robust negative correlation

281 between the rBC mass concentration and photochemical age. Compared to the in-plume segments of a

282 flight, the out-of-plume ones were characterized by not only lower rBC concentrations but also older

283 photochemical ages. Given the clear dependence of rBC concentration on photochemical age (Figure

284 6b) and the stable rBC size distribution across the whole rBC concentration range observed within an

285 emission flight (Figure 6a and Table 2), it could be inferred that rBC size distribution was independent

286 of photochemical age over the OS source region.

287 **3.3 rBC size distributions downwind of the OS source region**

288 Mass and number size distributions of rBC are shown in Figures 7 and 8, respectively, for the

289 transformation flight conducted on September 4, 2013 (i.e., F_9/4) which reached a downwind

290 distance of approximately 120 km (relative to the downwind edge of the OS source area; Figure 1b).

291 As can be seen from the time-resolved lognormal fitting results (Figures 7a and 8a), both the rBC

292 mass and number size distributions were fairly stable during F_9/4, without major temporal change

293 patterns. For the typical in- and out-of-plume conditions of F_9/4, the rBC MMD were 143 and 142

11

nm with mass distribution widths of 0.72 and 0.71, respectively (Figure 7b); the rBC NMD were 71

and 69 nm with number distribution widths of 0.68 and 0.69, respectively (Figure 8b). These rBC size

distributions (Figures 7b and 8b) were derived from the SP2 measurements performed on the various

virtual screens, where the aircraft was flown along level flight tracks (primarily at ~ 450 and 600 m)

perpendicular to the wind direction. For the level flight tracks, the typical in- and out-of-plume

conditions (i.e., segments) were distinguished by rBC concentration (Figure 9), i.e., the typical out-of-

plume conditions were identified by relatively low and constant rBC concentrations whereas the

typical in-plume conditions were characterized by sharp increases in rBC concentration above the out-

of-plume level. In Figure 7b, the rBC mass size distribution was scaled for the out-of-plume

conditions to reveal their lower rBC concentrations compared to the in-plume conditions (Figure 7d).

When performing the scaling, the in-plume rBC size distribution was used as a reference (i.e., kept

unchanged). The out-of-plume rBC size distribution was scaled to make the $I_{\text{out-of-plume, scaled}}$ to $I_{\text{in-plume}}$

ratio equal the $rBC_{\text{out-of-plume}}$ to $rBC_{\text{in-plume}}$ ratio, where the individual terms, in sequence, represent the

integral of the scaled out-of-plume rBC size distribution curve, the integral of the reference in-plume

rBC size distribution curve, the average out-of-plume rBC mass concentration (54 ng/m^3, derived

from Figure 7d), and the average in-plume rBC concentration (208 ng/m^3, derived from Figure 7d). In

Figure 8b, the out-of-plume rBC number size distribution was scaled similarly. As can be seen from

Figures 7b and 8b, the in- vs. out-of-plume difference was negligible for rBC size distribution

downwind of the OS region.

Photochemical ages were older for the out-of-plume conditions compared to the in-plume ones,

by ~ 0.3−0.5 in terms of $-\log_{10}(NO_x/NO_y)$ for different screens of F_9/4 (Figure 7e). Therefore, the

consistent rBC size distributions between the in- and out-of-plume conditions indicated that

photochemical age had little influence on rBC size distribution downwind of the OS region. This

conclusion was also strongly supported by the comparison of in-plume rBC size distributions among

different downwind distances. As the OS plume was transported downwind, the in-plume rBC

concentration decreased due to dilution (Figure 7d), from ~ 310 ng/m^3 for the first screen (screen #1)

to ~ 110 ng/m^3 for the fourth screen (screen #4); on the other hand, the in-plume photochemical age

321　$-\log_{10}(NO_x/NO_y)$ increased (Figure 7e), from ~ 0.1 for screen #1 to ~ 0.5 for screen #4. The last

322　screen (screen #5) did not differ largely from screen #4 with respect to either in-plume rBC

323　concentration or photochemical age, appearing to indicate that the dilution and aging processes had

324　slowed down or even stopped since screen #4. However, it should be noted that unlike the first four

325　screens, screen #5 did not captured the full OS plume, i.e., the plume edges were missed. Compared to

326　the central portion of the plume, the plume edges had lower rBC concentrations and older

327　photochemical ages. Therefore, the average rBC concentration and $-\log_{10}(NO_x/NO_y)$ could not be

328　compared directly between screen #5 and the first four screens, and consequently, results from screen

329　#5 were not involved in Figures 7d and 7e. Nonetheless, for all successive screens of F_9/4, the in-

330　plume rBC MMD and NMD were found to fall into a narrow range of 140−145 and 69−72 nm,

331　respectively, while both the mass and number distribution widths were about 0.7 (Figures 7c, 8c and

332　10). In Figures 7c and 8c, rBC size distributions derived from successive screens were scaled to reveal

333　the decrease in rBC concentration caused by dilution, using the same approach as that described in

334　detail for Figure 7b. The scaling requires rBC concentration representative for the full plume and thus

335　was not performed for screen #5. A direct comparison of rBC size distributions between screen #5 and

336　the first four screens is provided by Figure 10. Figure 10 also demonstrates consistent in-plume rBC

337　size distributions among successive screens for the other two transformation flights that were

338　conducted on August 19 and September 5, 2013, respectively (i.e., F_8/19 and F_9/5), providing

339　further solid evidence for the negligible influence of atmospheric aging on rBC size distribution

340　downwind of the OS source region.

341　As shown in Table 1, previous studies conducted in remote areas (either ground- or aircraft-based)

342　typically showed rBC MMD between 200 and 220 nm (Shiraiwa et al., 2008; Liu et al., 2010;

343　McMeeking et al., 2010; Schwarz et al., 2010), substantially higher than those observed over urban

344　areas (e.g., 122 nm over the Los Angeles basin; Metcalf et al., 2012) or at urban locations (e.g., 146

345　nm in Tokyo, Japan; Kondo et al., 2011b). Moreover, the rBC MMD was found to be 20 nm larger for

346　aged urban plumes from Nagoya, Japan compared to fresh emissions from the same urban area

347　(Moteki et al., 2007). Therefore, it has been argued that rBC size distribution tends to shift toward

larger sizes during aging (e.g., McMeeking et al., 2010). Results from the present study, especially the comparison of rBC size distributions among successive flight screens (Figure 10), indicate that this is not necessarily the case. It is inferred that not all aging processes will change rBC size distribution and instead, influences of aging on rBC size distribution may partially depend on the presence of atmospheric processes that can lead to increased rBC core mass and size in a single particle (e.g., rBC coagulation and evaporation of cloud droplets containing multiple rBC particles). In this study, it appears that no such processes were at play, and within the photochemical ages encountered, rBC core masses and sizes did not change.

In addition to the evolution of in-plume rBC concentration, Figure 7d shows that the out-of-plume rBC concentration decreased until screen #3. This decrease was associated with an increase in $-\log_{10}(NO_x/NO_y)$ for the out-of-plume conditions (Figure 7e). For screen #4, both the out-of-plume rBC concentration and photochemical age were nearly the same as the respective values observed for screen #3. Therefore, the out-of-plume conditions identified for screens #3 and #4 should be more representative of the background. For screens #3 and #4, rBC size distributions agreed well between the in- and out-of-plume conditions, within ± 3 nm in terms of MMD or NMD, indicating that the background did not differ significantly from the OS emissions with respect to rBC size distribution. Consistent in- and out-of-plume rBC size distributions observed at smaller downwind distances (i.e., for screens #1 and #2) and over the OS source area (i.e., for the emission flights) pointed to the same conclusion, although the out-of-plume conditions in these cases were less representative of the background. rBC cores in the background could be from the OS emissions and/or long-range transported urban emissions that had not been influenced by atmospheric processes that can change single particle rBC core size. These two kinds of emissions did not differ largely in rBC size distribution (as discussed in section 3.1) and therefore they were difficult to be further distinguished only by rBC size.

3.4 Evolution of rBC mixing state

Coating thickness ($T_{coating}$) was found to exhibit a decreasing trend with the increase in rBC D_{MEV} for both the transformation (Figure 11) and emission flights (Figure S4). This trend was primarily

14

375   attributed to the limitation that the detection range of $T_{coating}$ is rBC D_{MEV} dependent (as explained in

376   Section 2.3), rather than indicating that relatively small rBC cores were more thickly coated than

377   larger ones. Besides $T_{coating}$, the fraction of rBC cores that can be assigned a coating thickness ($F_{assigned}$,

378   in %) was also rBC D_{MEV} dependent such that $F_{assigned}$ was found to be the highest (between ~

379   35−45%) for rBC cores in the D_{MEV} range of 130−160 nm (Figure 11 and Figure S4). The rBC

380   containing particles in this D_{MEV} range were selected for further discussions on $T_{coating}$ (their $T_{coating}$

381   will be specified as T^*), with a focus on the evolution of rBC mixing state as the OS plumes were

382   transported downwind.

383   As shown in Figure 12a for the transformation flight F_9/4, the in-plume T^* exhibited an

384   increasing trend with the increase in downwind distance or transport time, e.g., from ~ 22 nm for

385   screen #1 to ~ 41 nm for screen #4. This trend is not surprising given the continuous formation of

386   SOA during transport of the OS plumes (Liggio et al., 2016). For rBC near the sources, T^* was close

387   to zero as observed from the emission flights over the OS facilities. For example, T^* was derived at ~

388   3 nm for F_9/3 (Figure S4). These freshly emitted rBC cores grew a coating of ~ 20 nm thickness in

389   the first hour after emission, when the OS plume was transported from the sources in the OS facilities

390   to the downwind edge of the OS region.

391   T^* were found to be comparable between the in- and out-of-plume conditions for screen #1,

392   which were ~ 22 and 23 nm, respectively (Figure 12a). It is unlikely that the out-of-plume T^* could be

393   as low was ~ 23 nm, if the majority of the out-of-plume rBC cores were from long-range transport.

394   Therefore, the rBC cores observed in the out-of-plume conditions should also be influenced by

395   emissions in the oil sands region albeit at much lower air concentrations compared to the plumes, such

396   as from on road traffic that was not part of any oil sands surface mining facility.

397   Compared to in plumes, the increase in T^* was smaller for the out-of-plume conditions as the OS

398   plume was further transported from screen #1 (Figure 12a) and moreover, the out-of-plume T^*

399   stopped increasing after screen #3 such that it was ~ 32 nm for both screens #3 and #4. One

400   explanation for the different evolution patterns of the in- and out-of-plume T^*, which had comparable

401   initial values (i.e., those for screen #1), is the less effective formation of coating materials (e.g., SOA

402 and sulfate) for the out-of-plume conditions than in plumes. Coating precursors (volatile organic

403 compounds and sulfur dioxide) were much more abundant in the plumes, from which fast formation of

404 SOA was observed (Liggio et al., 2016). As shown in Figure 12b, the in-plume OA to rBC mass ratio

405 exhibited a robust increasing trend with the increase in downwind distance (e.g., by ~ 150% for screen

406 #4 relative to screen #1), whereas the increase in OA to rBC ratio was less significant for the out-of-

407 plume conditions (e.g., by only ~ 45% for screen #4 compared to screen #1) which was negligible

408 between screens #3 and #4.

409 We did not compare $T_{coating}$ measured in this study with results from previous ones due to the

410 following reasons. (1) The detection range of $T_{coating}$ and therefore the estimated $T_{coating}$ depend on the

411 SP2's detection range of scattering intensity, which could differ among different SP2 instruments.

412 This dependency indicates that different SP2 instruments might lead to different $T_{coating}$ estimates even

413 for the same ensemble of rBC containing particles. (2) The detection range of $T_{coating}$ and therefore the

414 estimated $T_{coating}$ also depend on the rBC core size (i.e., D_{MEV}). Quite different D_{MEV} ranges have been

415 used by previous studies to estimate $T_{coating}$, e.g., 190−210 nm by Schwarz et al. (2008a, b) vs.

416 162−185 nm by Langridge et al. (2012), indicating that these $T_{coating}$ estimates are not directly

417 comparable. (3) Comparison of the LEO and full-Gaussian fits for the determination of $D_{optical}$ or

418 scattering amplitude, which should be done using non-rBC containing particles, was not presented in

419 many previous publications reporting $T_{coating}$. This is a concern because the LEO fit has been

420 considered reliable as long as the LEO to full-Gaussian ratios are relatively constant (not necessarily

421 around 1.0) for the fitted scattering amplitudes (e.g., Metcalf, et al., 2010). Since an agreement

422 between the LEO and full-Gaussian fits was not always required, previously reported $T_{coating}$ might be

423 biased by the LEO-induced uncertainty to different extents, adding to the difficulties in comparing

424 $T_{coating}$ across studies.

425 **4. Conclusions**

426 An aircraft campaign was conducted over the Athabasca oil sands region in the summer of 2013,

427 during which the size distribution and coating thickness of refractive black carbon (rBC) cores were

428 studied as they were emitted from the sources and as they were transported downwind. The rBC size

16

429   distributions were found to be comparable at the six major OS surface mining facilities, typically with

430   mass median diameters (MMD) of 135–145 nm and number median diameters (NMD) of 60–70 nm

431   that were characteristic of fresh urban emissions dominated by contributions from fossil fuel

432   combustion. The observed rBC size distributions were consistent (in terms of MMD, NMD and the

433   corresponding distribution widths) not only for the typical in- and out-of-plume segments of a flight

434   but also for different downwind distances from the OS source area, indicating little dependence of the

435   rBC size distribution on atmospheric aging within 4 to 5 hours from the point of emission.

436   The coating thicknesses ($T_{coating}$) were retrieved for rBC containing particles from their scattering

437   signals, on a particle-by-particle basis. The uncertainty of the LEO fit, a key step to compute $T_{coating}$,

438   was evaluated using non-rBC containing particles. The LEO fit and the reference full-Gaussian fit

439   were found to agree within approximately ± 15% in determining the optical size of non-rBC

440   containing particles. Mainly due to the SP2's limited detection range of scattering intensity, however,

441    $T_{coating}$ could not be calculated for all the detected rBC cores. The fraction of rBC cores that can be

442   assigned a coating thickness was found to be the highest but still lower than 50% for those in the

443   diameter range of 130−160 nm. It is not surprising that $T_{coating}$ increased as the OS plumes were

444   transported downwind, resulting from the formation mainly of secondary organic aerosols but also of

445   sulfate. Such coating increase with aging can significantly change the optical properties of the rBC

446   containing particles and hence their potentials for radiative forcing. Therefore, to resolve the coating

447   impact on rBC radiative forcing, secondary organic aerosol and sulfate on the global basis need to be

448   well quantified along with accurately determined black carbon emission rates.

449   **Acknowledgements**

454   **References**

455   Alberta Energy: Oil Sands Production Profile: 2004-2014, ISBN: 978-1-4601-2723-0, 2016.

17

456   Alberta Energy: Oil Sands Facts and Statistics, available at

457   http://www.energy.alberta.ca/OilSands/791.asp, last accessed on March 28, 2017.

458   Andreae, M. O. and Gelencsér, A.: Black carbon or brown carbon? The nature of light-absorbing

459   carbonaceous aerosols, Atmos. Chem. Phys., 6, 3131–3148, 2006.

460   Baumgardner, D., Kok, G., and Raga, G.: Warming of the Arctic lower stratosphere by light absorbing

461   particles, Geophys. Res. Lett., 31, L06117, doi:10.1029/2003GL018883, 2004.

462   Bond, T. C. and Bergstrom, R. W.: Light absorption by carbonaceous particles: an investigative

463   review, Aerosol Sci. Technol., 40, 27–67, 2006.

464   Bond, T. C., Doherty, S. J., Fahey, D. W., Forster, P. M., Berntsen, T., DeAngelo, B. J., Flanner, M.

465   G., Ghan, S., Kärcher, B., Koch, D., Kinne, S., Kondo, Y., Quinn, P. K., Sarofim, M. C., Schultz,

466   M. G., Schulz, M., Venkataraman, C., Zhang, H., Zhang, S., Bellouin, N., Guttikunda, S. K.,

467   Hopke, P. K., Jacobson, M. Z., Kaiser, J. W., Klimont, Z., Lohmann, U., Schwarz, J. P., Shindell,

468   D., Storelvmo, T., Warren, S. G., and Zender, C. S.: Bounding the role of black carbon in the

469   climate system: a scientific assessment, J. Geophys. Res., 118, 5380–5552,

470   doi:10.1002/jgrd.50171, 2013.

471   Buffaloe, G. M., Lack, D. A., Williams, E. J., Coffman, D., Hayden, K. L., Lerner, B. M., Li, S. M.,

472   Nuaaman, I., Massoli, P., Onasch, T. B., Quinn, P. K., and Cappa, C. D.: Black carbon emissions

473   from in-use ships: a California regional assessment, Atmos. Chem. Phys., 14, 1881–1896, 2014.

474   Buseck, P. R., Adachi, K., Gelencsér, A., Tompa, É., and Pósfai, M.: Ns-Soot: a material-based term

475   for strongly light-absorbing carbonaceous particles, Aerosol Sci. Technol., 48, 777–788, 2014.

476   Cappa, C. D., Onasch, T. B., Massoli, P., Worsnop, D. R., Bates, T. S., Cross, E. S., Davidovits, P.,

477   Hakala, J., Hayden, K. L., Jobson, B. T., Kolesar, K. R., Lack, D. A., Lerner, B. M., Li, S. M.,

478   Mellon, D., Nuaaman, I., Olfert, J. S., Petäjä, T., Quinn, P. K., Song, C., Subramanian, R.,

479   Williams, E. J., and Zaveri, R. A.: Radiative absorption enhancements due to the mixing state of

480   atmospheric black carbon, Science, 337, 1078–1081, 2012.

481   Dahlkötter, F., Gysel, M., Sauer, D., Minikin, A., Baumann, R., Seifert, P., Ansmann, A., Fromm, M.,

482   Voigt, C., and Weinzierl, B.: The Pagami Creek smoke plume after long-range transport to the

18

483   upper troposphere over Europe – aerosol properties and black carbon mixing state, Atmos. Chem.

484   Phys., 14, 6111–6137, 2014.

485   Dentener, F., Kinne, S., Bond, T., Boucher, O., Cofala, J., Generoso, S., Ginoux, P., Gong, S.,

486   Hoelzemann, J. J., Ito, A., Marelli, L., Penner, J. E., Putaud, J. P., Textor, C., Schulz, M., van der

487   Werf, G. R., and Wilson, J.: Emissions of primary aerosol and precursor gases in the years 2000

488   and 1750 prescribed data-sets for AeroCom, Atmos. Chem. Phys., 6, 4321–4344, 2006.

489   Gao, R. S., Schwarz, J. P., Kelly, K. K., Fahey, D. W., Watts, L. A., Thompson, T. L., Spackman, J.

490   R., Slowik, J. G., Cross, E. S., Han, J. H., Davidovits, P., Onasch, T. B., and Worsnop, D. R.: A

491   novel method for estimating light-scattering properties of soot aerosols using a modified Single-

492   Particle Soot Photometer, Aerosol Sci. Technol., 41, 125–135, 2007.

493   Gordon, M., Li, S. M., Staebler, R., Darlington, A., Hayden, K., O'Brien, J., and Wolde, M.:

494   Determining air pollutant emission rates based on mass balance using airborne measurement data

495   over the Alberta oil sands operations, Atmos. Meas. Tech., 8, 3745–3765, 2015.

496   Government of Alberta: Environmental Management of Alberta's Oil Sands, ISBN: 978-0-7785-7677-

497   8, 2009.

498   Heald, C. L., Ridley, D. A., Kroll, J. H., Barrett, S. R. H., Cady-Pereira, K. E., Alvarado, M. J., and

499   Holmes, C. D.: Contrasting the direct radiative effect and direct radiative forcing of aerosols,

500   Atmos. Chem. Phys., 14, 5513–5527, 2014.

501   Huebert, B. J., Howell, S. G., Covert, D., Bertram, T., Clarke, A., Anderson, J. R., Lafleur, B. G.,

502   Seebaugh, W. R., Wilson, J. C., Gesler, D., Blomquist, B., and Fox, J.: PELTl: measuring the

503   passing efficiency of an airborne low turbulence aerosol inlet, Aerosol Sci. Technol., 38, 803–826,

504   2004.

505   IPCC, 2013: Climate Change 2013: The Physical Science Basis. Contribution of Working Group I to

506   the Fifth Assessment Report of the Intergovernmental Panel on Climate Change, edited by:

507   Stocker, T. F., Qin, D., Plattner, G. K., Tignor, M., Allen, S. K., Boschung, J., Nauels, A., Xia, Y.,

508   Bex, V., and Midgley, P. M., Cambridge University Press, Cambridge, United Kingdom and New

509   York, NY, USA.

510   Kelly, E. N., Schindler, D. W., Hodson, P. V., Short, J. W., Radmanovich, R., and Nielsen, C. C.: Oil

511   sands development contributes elements toxic at low concentrations to the Athabasca River and

512   its tributaries, Proc. Natl. Acad. Sci. U.S.A., 107, 16178–16183, 2010.

513   Kelly, E. N., Short, J. W., Schindler, D. W., Hodson, P. V., Ma, M., Kwan, A. K., and Fortin, B. L.:

514   Oil sands development contributes polycyclic aromatic compounds to the Athabasca River and its

515   tributaries, Proc. Natl. Acad. Sci. U.S.A., 106, 22346–22351, 2009.

516   Kleinman, L. I., Springston, S. R., Daum, P. H., Lee, Y. N., Nunnermacker, L. J., Senum, G. I., Wang,

517   J., Weinstein-Lloyd, J., Alexander, M. L., Hubbe, J., Ortega, J., Canagaratna, M. R., and Jayne, J.:

518   The time evolution of aerosol composition over the Mexico City plateau, Atmos. Chem. Phys., 8,

519   1559–1575, 2008.

520   Kondo, Y., Matsui, H., Moteki, N., Sahu, L., Takegawa, N., Kajino, M., Zhao, Y., Cubison, M. J.,

521   Jimenez, J. L., Vay, S., Diskin, G. S., Anderson, B., Wisthaler, A., Mikoviny, T., Fuelberg, H. E.,

522   Blake, D. R., Huey, G., Weinheimer, A. J., Knapp, D. J., and Brune, W. H.: Emissions of black

523   carbon, organic, and inorganic aerosols from biomass burning in North America and Asia in 2008,

524   J. Geophys. Res., 116, D08204, doi:10.1029/2010JD015152, 2011a.

525   Kondo, Y., Sahu, L., Moteki, N., Khan, F., Takegawa, N., Liu, X., Koike, M., and Miyakawa, T.:

526   Consistency and traceability of black carbon measurements made by laser-induced incandescence,

527   thermal-optical transmittance, and filter-based photo-absorption techniques, Aerosol Sci.

528   Technol., 45, 295–312, 2011b.

529   Kurek, J., Kirk, J. L., Muir, D. C. G., Wang, X., Evans, M. S., and Smol, J. P.: Legacy of a half

530   century of Athabasca oil sands development recorded by lake ecosystems, Proc. Natl. Acad. Sci.

531   U.S.A., 110, 1761–1766, 2013.

532   Laborde, M., Crippa, M., Tritscher, T., Jurányi, Z., Decarlo, P. F., Temime-Roussel, B., Marchand, N.,

533   Eckhardt, S., Stohl, A., Baltensperger, U., Prévôt, A. S. H., Weingartner, E., and Gysel, M.:

534   Black carbon physical properties and mixing state in the European megacity Paris, Atmos. Chem.

535   Phys., 13, 5831–5856, 2013.

536   Laborde, M., Mertes, P., Zieger, P., Dommen, J., Baltensperger, U., and Gysel, M.: Sensitivity of the

537   Single Particle Soot Photometer to different black carbon types, Atmos. Meas. Tech., 5, 1031–

538   1043, 2012a.

539   Laborde, M., Schnaiter, M., Linke, C., Saathoff, H., Naumann, K. H., Möhler, O., Berlenz, S., Wagner,

540   U., Taylor, J. W., Liu, D., Flynn, M., Allan, J. D., Coe, H., Heimerl, K., Dahlkötter, F., Weinzierl,

541   B., Wollny, A. G., Zanatta, M., Cozic, J., Laj, P., Hitzenberger, R., Schwarz, J. P., and Gysel, M.:

542   Single Particle Soot Photometer intercomparison at the AIDA chamber, Atmos. Meas. Tech., 5,

543   3077–3097, 2012b.

544   Lambe, A. T., Cappa, C. D., Massoli, P., Onasch, T. B., Forestieri, S. D., Martin, A. T., Cummings, M.

545   J., Croasdale, D. R., Brune,W. H.,Worsnop, D. R., and Davidovits, P.: Relationship between

546   oxidation level and optical properties of secondary organic aerosol, Environ. Sci. Technol., 47,

547   6349–6357, 2013.

548   Langridge, J. M., Lack, D., Brock, C. A., Bahreini, R., Middlebrook, A. M., Neuman, J. A., Nowak, J.

549   B., Perring, A. E., Schwarz, J. P., Spackman, J. R., Holloway, J. S., Pollack, I. B., Ryerson, T. B.,

550   Roberts, J. M., Warneke, C., de Gouw, J. A., Trainer, M. K., and Murphy, D. M.: Evolution of

551   aerosol properties impacting visibility and direct climate forcing in an ammonia-rich urban

552   environment, J. Geophys. Res., 117, D00V11, doi:10.1029/2011JD017116, 2012.

553   Li, S. M., Leithead, A., Moussa, S. G., Liggio, J., Moran, M. D., Wang, D., Hayden, K., Darlington,

554   A., Gordon, M, Staebler, R., Makar, P. A., Stroud, C. A., McLaren, R., Liu, P., O'Brien, J.,

555   Mittermeier, R. L., Zhang, J., Marson, G., Cober, S. G., Wolde, M., and Wentzell, J.: Differences

556   between measured and reported volatile organic compound emissions from oil sands facilities in

557   Alberta, Canada, Proc. Natl. Acad. Sci. U.S.A., 114, E3756–E3765, 2017.

558   Liggio, J., Gordon, M., Smallwood, G., Li, S. M., Stroud, C., Staebler, R., Lu, G., Lee, P., Taylor, B.,

559   and Brook, J. R.: Are emissions of black carbon from gasoline vehicles underestimated? Insights

560   from near and on-road measurements, Environ. Sci. Technol., 46, 4819–4828, 2012.

561   Liggio, J., Li, S. M., Hayden, K., Taha, Y. M., Stroud, C., Darlington, A., Drollette, B. D., Gordon, M.,

562   Lee, P., Liu, P., Leithead, A., Moussa, S. G., Wang, D., O'Brien, J., Mittermeier, R. L., Brook, J.

563   R., Lu, G., Staebler, R. M., Han, Y., Tokarek, T. W., Osthoff, H. D., Makar, P. A., Zhang, J.,

564   Plata, D. L., and Gentner, D. R.: Oil sands operations as a large source of secondary organic

565   aerosols, Nature, 534, 91–94, 2016.

566   Liggio, J., Moussa, S. G., Wentzell, J., Darlington, A., Liu, P., Leithead, A., Hayden, K., O'Brien, J.,

567   Mittermeier, R. L., Staebler, R., Wolde, M., and Li, S. M.: Understanding the primary emissions

568   and secondary formation of gaseous organic acids in the oil sands region of Alberta, Canada,

569   Atmos. Chem. Phys., 17, 8411-8427, 2017.

570   Liu, D., Allan, J. D., Young, D. E., Coe, H., Beddows, D., Fleming, Z. L., Flynn, M. J., Gallagher, M.

571   W., Harrison, R. M., Lee, J., Prevot, A. S. H., Taylor, J. W., Yin, J., Williams, P. I., and Zotter, P.:

572   Size distribution, mixing state and source apportionment of black carbon aerosol in London

573   during wintertime, Atmos. Chem. Phys., 14, 10061–10084, 2014.

574   Liu, D., Flynn, M., Gysel, M., Targino, A., Crawford, I., Bower, K., Choularton, T., Jurányi, Z.,

575   Steinbacher, M., Hüglin, C., Curtius, J., Kampus, M., Petzold, A., Weingartner, E., Baltensperger,

576   U., and Coe, H.: Single particle characterization of black carbon aerosols at a tropospheric alpine

577   site in Switzerland, Atmos. Chem. Phys., 10, 7389–7407, 2010.

578   McMeeking, G. R., Hamburger, T., Liu, D., Flynn, M., Morgan, W. T., Northway, M., Highwood, E.

579   J., Krejci, R., Allan, J. D., Minikin, A., and Coe, H.: Black carbon measurements in the boundary

580   layer over western and northern Europe, Atmos. Chem. Phys., 10, 9393–9414, 2010.

581   Metcalf, A. R., Craven, J. S., Ensberg, J. J., Brioude, J., Angevine, W., Sorooshian, A., Duong, H. T.,

582   Jonsson, H. H., Flagan, R. C., and Seinfeld, J. H.: Black carbon aerosol over the Los Angeles

583   Basin during CalNex, J. Geophys. Res., 117, D00V13, doi:10.1029/2011JD017255, 2012.

584   Morgenstern, O., Hegglin, M. I., Rozanov, E., O'Connor, F. M., Abraham, N. L., Akiyoshi, H.,

585   Archibald, A. T., Bekki, S., Butchart, N., Chipperfield, M. P., Deushi, M., Dhomse, S. S., Garcia,

586   R. R., Hardiman, S. C., Horowitz, L. W., Jöckel, P., Josse, B., Kinnison, D., Lin, M., Mancini, E.,

587   Manyin, M. E., Marchand, M., Maréca, V., Michou, M., Oman, L. D., Pitari, G., Plummer, D. A.,

588   Revel, L. E., Saint-Martin, D., Schofield, R., Stenke, A., Stone, K., Sudo, K., Tanaka, T. Y.,

589   Tilmes, S., Yamashita, Y., Yoshida, K., and Zeng, G.: Review of the global models used within

590   phase 1 of the Chemistry–Climate Model Initiative (CCMI), Geosci. Model Dev., 10, 639–671,

591   2017.

592 Moteki, N. and Kondo, Y.: Dependence of laser-induced incandescence on physical properties of

593   black carbon aerosols: measurements and theoretical interpretation, Aerosol Sci. Technol., 44,

594   663–675, 2010.

595 Moteki, N., Kondo, Y., Miyazaki, Y., Takegawa, N., Komazaki, Y., Kurata, G., Shirai, T., Blake, D.

596   R., Miyakawa, T., and Koike, M.: Evolution of mixing state of black carbon particles: aircraft

597   measurements over the western Pacific in March 2004, Geophys. Res. Lett., 34, L11803,

598   doi:10.1029/2006GL028943, 2007.

599 Moteki, N., Kondo, Y., and Nakamura, S.: Method to measure refractive indices of small nonspherical

600   particles: application to black carbon particles, J. Aerosol Sci., 41, 513–521, 2010.

601 Myhre, G., Samset, B. H., Schulz, M., Balkanski, Y., Bauer, S., Berntsen, T. K., Bian, H., Bellouin, N.,

602   Chin, M., Diehl, T., Easter, R. C., Feichter, J., Ghan, S. J., Hauglustaine, D., Iversen, T., Kinne,

603   S., Kirkevåg, A., Lamarque, J. F., Lin, G., Liu, X., Lund, M. T., Luo, G., Ma, X., van Noije, T.,

604   Penner, J. E., Rasch, P. J., Ruiz, A., Seland, Ø., Skeie, R. B., Stier, P., Takemura, T., Tsigaridis,

605   K., Wang, P., Wang, Z., Xu, L., Yu, H., Yu, F., Yoon, J. H., Zhang, K., Zhang, H., and Zhou, C.:

606   Radiative forcing of the direct aerosol effect from AeroCom Phase II simulations, Atmos. Chem.

607   Phys., 13, 1853–1877, 2013.

608 Parajulee, A. and Wania, F.: Evaluating officially reported polycyclic aromatic hydrocarbon emissions

609   in the Athabasca oil sands region with a multimedia fate model, Proc. Natl. Acad. Sci. U.S.A.,

610   111, 3344–3349, 2014.

611 Petzold, A., Ogren, J. A., Fiebig, M., Laj, P., Li, S. M., Baltensperger, U., Holzer-Popp, T., Kinne, S.,

612   Pappalardo, G., Sugimoto, N., Wehrli, C., Wiedensohler, A., and Zhang, X. Y.:

613   Recommendations for reporting "black carbon" measurements, Atmos. Chem. Phys., 13, 8365–

614   8379, 2013.

615 Ramanathan, V. and Carmichael G.: Global and regional climate changes due to black carbon, Nature

616   Geosci., 1, 221–227, 2008.

617   Sahu, L. K., Kondo, Y., Moteki, N., Takegawa, N., Zhao, Y., Cubison, M. J., Jimenez, J. L., Vay, S.,

618   Diskin, G. S., Wisthaler, A., Mikoviny, T., Huey, L. G., Weinheimer, A. J., and Knapp, D. J.:

619   Emission characteristics of black carbon in anthropogenic and biomass burning plumes over

620   California during ARCTAS-CARB 2008, J. Geophys. Res., 117, D16302,

621   doi:10.1029/2011JD017401, 2012.

622   Samset, B. H., Myhre, G., Herber, A., Kondo, Y., Li, S. M., Moteki, N., Koike, M., Oshima, N.,

623   Schwarz, J. P., Balkanski, Y., Bauer, S. E., Bellouin, N., Berntsen, T. K., Bian, H., Chin, M.,

624   Diehl, T., Easter, R. C., Ghan, S. J., Iversen, T., Kirkevåg, A., Lamarque, J. F., Lin, G., Liu, X.,

625   Penner, J. E., Schulz, M., Seland, Ø., Skeie, R. B., Stier, P., Takemura, T., Tsigaridis, K., and

626   Zhang, K.: Modelled black carbon radiative forcing and atmospheric lifetime in AeroCom Phase

627   II constrained by aircraft observations, Atmos. Chem. Phys., 14, 12465–12477, 2014.

628   Schnaiter, M., Linke, C., Möhler, O., Naumann, K. H., Saathoff, H., Wagner, R., Schurath, U.,

629   Wehner, B.: Absorption amplification of black carbon internally mixed with secondary organic

630   aerosol, J. Geophys. Res., 110, D19204. http://dx.doi.org/10.1029/2005JD006046, 2005.

631   Schwarz, J. P., Gao, R. S., Fahey, D. W., Thomson, D. S., Watts, L. A., Wilson, J. C., Reeves, J. M.,

632   Darbeheshti, M., Baumgardner, D. G., Kok, G. L., Chung, S. H., Schulz, M., Hendricks, J., Lauer,

633   A., Karcher, B., Slowik, J. G., Rosenlof, K. H., Thompson, T. L., Langford, A. O., Loewenstein,

634   M., and Aikin, K. C.: Single-particle measurements of midlatitude black carbon and light-

635   scattering aerosols from the boundary layer to the lower stratosphere, J. Geophys. Res., 111,

636   D16207, doi:10.1029/2006JD007076, 2006.

637   Schwarz, J. P., Gao, R. S., Spackman, J. R., Watts, L. A., Thomson, D. S., Fahey, D. W., Ryerson, T.

638   B., Peischl, J., Holloway, J. S., Trainer, M., Frost, G. J., Baynard, T., Lack, D. A., de Gouw, J. A.,

639   Warneke, C., and Del Negro, L. A.: Measurement of the mixing state, mass, and optical size of

640   individual black carbon particles in urban and biomass burning emissions, Geophys. Res. Lett.,

641   35, L13810, doi:10.1029/2008GL033968, 2008a.

642   Schwarz, J. P., Spackman, J. R., Fahey, D. W., Gao, R. S., Lohmann, U., Stier, P., Watts, L. A.,

643   Thomson, D. S., Lack, D. A., Pfister, L., Mahoney, M. J., Baumgardner, D., Wilson, J. C., and

644   Reeves, J. M.: Coatings and their enhancement of black carbon light absorption in the tropical

645   atmosphere, J. Geophys. Res., 113, D03203, doi:10.1029/2007JD009042, 2008b.

646 Schwarz, J. P., Spackman, J. R., Gao, R. S., Watts, L. A., Stier, P., Schulz, M., Davis, S. M., Wofsy, S.

647   C., and Fahey, D. W., Global-scale black carbon profiles observed in the remote atmosphere and

648   compared to models, Geophys. Res. Lett., 37, L18812, doi:10.1029/2010GL044372, 2010.

649 Shephard, M. W., McLinden, C. A., Cady-Pereira, K. E., Luo, M., Moussa, S. G., Leithead, A., Liggio,

650   J., Staebler, R. M., Akingunola, A., Makar, P., Lehr, P., Zhang, J., Henze, D. K., Millet, D. B.,

651   Bash, J. O., Zhu, L., Wells, K. C., Capps, S. L., Chaliyakunnel, S., Gordon, M., Hayden, K.,

652   Brook, J. R., Wolde, M., and Li, S. M.: Tropospheric Emission Spectrometer (TES) satellite

653   observations of ammonia, methanol, formic acid, and carbon monoxide over the Canadian oil

654   sands: validation and model evaluation, Atmos. Meas. Tech., 8, 5189–5211, 2015.

655 Shiraiwa, M., Kondo, Y., Moteki, N., Takegawa, N., Miyazaki, Y., and Blake, D. R.: Evolution of

656   mixing state of black carbon in polluted air from Tokyo, Geophys. Res. Lett., 34, L16803,

657   doi:10.1029/2007GL029819, 2007.

658 Shiraiwa, M., Kondo, Y., Moteki, N., Takegawa, N., Sahu, L. K., Takami, A., Hatakeyama, S.,

659   Yonemura, S., and Blake, D. R.: Radiative impact of mixing state of black carbon aerosol in

660   Asian outflow, J. Geophys. Res., 113, D24210, doi:10.1029/2008JD010546, 2008.

661 Stephens, M., Turner, N., and Sandberg, J.: Particle identification by laser-induced incandescence in a

662   solid-state laser cavity, Appl. Opt., 42, 3726–3736, 2003.

663 Stier, P., Feichter, J., Kinne, S., Kloster, S., Vignati, E., Wilson, J., Ganzeveld, L., Tegen, I., Werner,

664   M., Balkanski, Y., Schulz, M., Boucher, O., Minikin, A., and Petzold, A.: The aerosol-climate

665   model ECHAM5-HAM, Atmos. Chem. Phys., 5, 1125–1156, 2005.

666 Taylor, J. W., Allan, J. D., Allen, G., Coe, H., Williams, P. I., Flynn, M. J., Le Breton, M., Muller, J.

667   B. A., Percival, C. J., Oram, D., Forster, G., Lee, J. D., Rickard, A. R., Parrington, M., and

668   Palmer, P. I.: Size-dependent wet removal of black carbon in Canadian biomass burning plumes,

669   Atmos. Chem. Phys., 14, 13755–13771, 2014.

670   Taylor, J. W., Allan, J. D., Liu, D., Flynn, M., Weber, R., Zhang, X., Lefer, B. L., Grossberg, N.,

671   Flynn, J., and, Coe, H.: Assessment of the sensitivity of core/shell parameters derived using the

672   single-particle soot photometer to density and refractive index, Atmos. Meas. Tech., 8, 1701–

673   1718, 2015.

Table 1. A summary of rBC MMD representative for different types of emission sources. The calibration material and assumed density of rBC are also shown. rBC NMD are presented in parentheses when available.

Campaign information	Calibration material	Density (g/cm^3)	MMD (nm)	Reference
Urban emissions dominated by contributions from fossil fuel combustion				
Airborne measurement over California, USA in May 2010	Aquadag	1.8	122 over the Los Angeles basin (NMD ≈ 60 nm)	Metcalf et al. (2012)
Ground-based measurement downwind of Tokyo, Japan in the summer of 2004	thermal-denuded ambient soot	1.77	between 145 and 150	Shiraiwa et al. (2007)
Airborne measurement over Texas, USA in September 2006	glassy carbon spheres	2.0	~ 170 for urban emissions (NMD ≈ 70 nm)	Schwarz et al. (2008a)
Airborne measurement over California, USA in June 2008	thermal-denuded ambient soot	2.0	averaging 175 for urban emissions	Sahu et al. (2012)
Airborne measurement over Western and northern Europe in April and May 2008	Aquadag	1.8	173 and 178 for urban outflows from Liverpool, UK and Cabauw, Netherlands, respectively (NMD ≈ 80 nm for both cases)	McMeeking et al. (2010)
Ground-based measurement in Paris, France during the winter of 2010	fullerene soot	1.8	~ 100 when impacted by fresh traffic emissions	Laborde et al. (2013)
Ground-based measurement in London, UK during the winter and summer of 2008	Aquadag	1.8	between 119 and 124 during summer when mainly impacted by traffic emissions	Liu et al. (2014)
Ground-based measurement in Tokyo, Japan from late August to early September 2009	thermal-denuded ambient soot	1.72	averaging 146, typically in the range of 130−170 (NMD averaging 64 nm)	Kondo et al. (2011b)
Ground-based measurement in Sacramento, USA in June 2010	Aquadag	1.8	~ 145	Cappa et al. (2012)

Near-source measurement at the Cranfield airport, UK in September 2008	Aquadag	1.8	126	McMeeking et al. (2010)
Laboratory study for source emissions from a diesel car	fullerene soot	1.8	~ 125	Laborde et al. (2012b)

Biomass burning emissions

Airborne measurement over Texas, USA in September 2006	glassy carbon spheres	2.0	~ 210 for biomass burning plumes (NMD ≈ 140 nm)	Schwarz et al. (2008a)
Airborne measurement over California, USA in June 2008	thermal-denuded ambient soot	2.0	averaging 193 for biomass burning plumes (NMD averaging 141 nm)	Sahu et al. (2012)
Airborne measurements over Canada between June and July 2008, and over the Arctic in April 2008	thermal-denuded ambient soot	2.0	187 for fresh biomass burning plumes in Canada (NMD = 136 nm); 207 for aged biomass burning plumes transported from Asia to the Arctic (NMD = 141 nm)	Kondo et al. (2011a)
Airborne measurement over Eastern Canada in July 2011	Aquadag	1.8	194 and 196 for two biomass burning plumes not impacted by wet deposition (NMD = 137 and 128 nm, respectively); 152 for a biomass burning plume impacted by wet deposition (NMD = 100 nm)	Taylor et al. (2014)

Aged air masses in remote areas

Ground-based measurement at a remote island in Japan during the spring of 2007	thermal-denuded ambient soot	1.77	between 200 and 220 (NMD between 120 and 140 nm)	Shiraiwa et al. (2008)
Ground-based measurement at a tropospheric site in Switzerland from February to March 2007	glassy carbon spheres	1.9	~ 200	Liu et al. (2010)
Airborne measurement over Western and northern Europe in April and May 2008	Aquadag	1.8	199 over the Atlantic Ocean (NMD ≈ 90 nm)	McMeeking et al. (2010)

Airborne measurement over the remote Pacific in January 2009	fullerene soot	2.0	~ 180 for remote atmosphere and ~ 225 for the Arctic	Schwarz et al. (2010b)

Table 2. Variations of the parameters derived from time-resolved lognormal fits to single-particle rBC data measured during F_8/26 and F_8/28. Variations are determined as relative standard deviations (RSD, in %).

	MMD	$\text{Width}_{\text{mass}}$	$F_{\text{rBC, mass}}$	NMD	$\text{Width}_{\text{number}}$	$F_{\text{rBC, number}}$
F_8/26	1.46	4.42	2.82	4.48	5.30	4.07
F_8/28	6.85	8.46	9.47	7.94	7.18	8.07
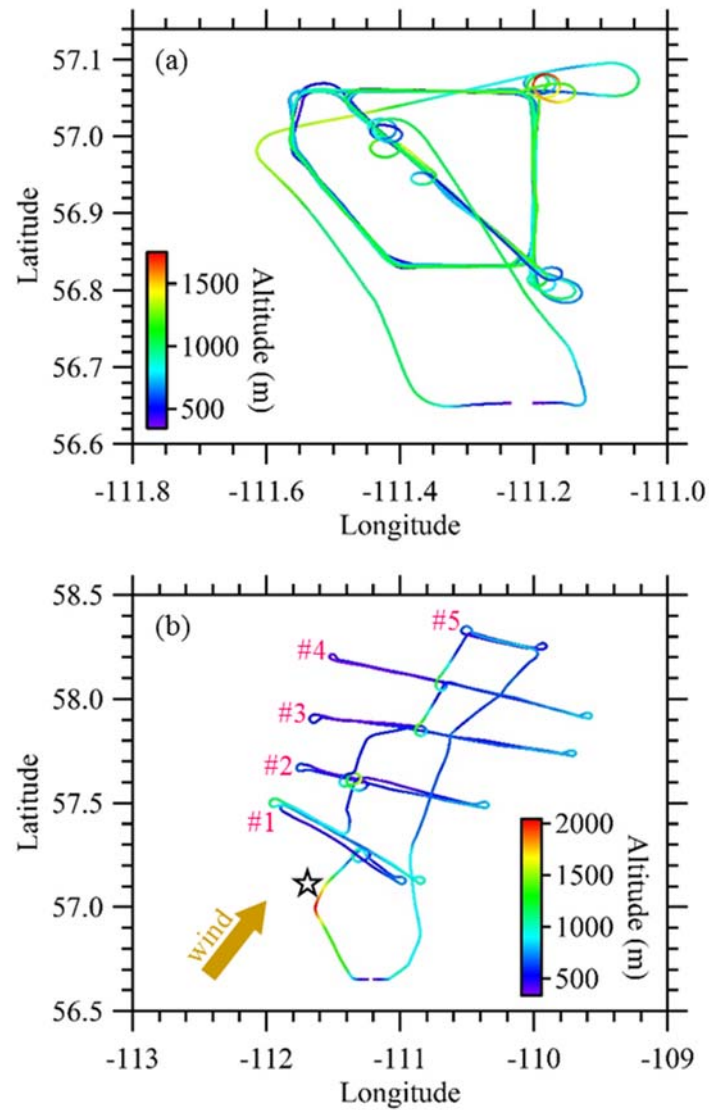
Figure 1. Examples of flight tracks for **(a)** emission and **(b)** transformation flights, which were flown on August 28 (F_8/28) and September 4 (F_9/4), 2013, respectively. F_8/28 was flown in a 5-sided polygon pattern, encircling the SUN facility. F_9/4 was conducted in a Lagrangian pattern, involving five virtual screens (#1 to #5). A virtual screen corresponds to a specific downwind distance from the OS source area and consists of level flight tracks perpendicular to the wind direction at multiple altitudes. Distances between the successive flight screens during F_9/4 were approximately 30 km, whereas distance between the OS center (shown approximately by the open star) and the first screen (i.e., screen #1 which was located at the downwind edge of the OS source region) was also about 30 km. Composite Google Earth images showing flight tracks are presented in Figure S1 for F_8/28 and F_9/4. Altitude shown here indicates the ellipsoid height.
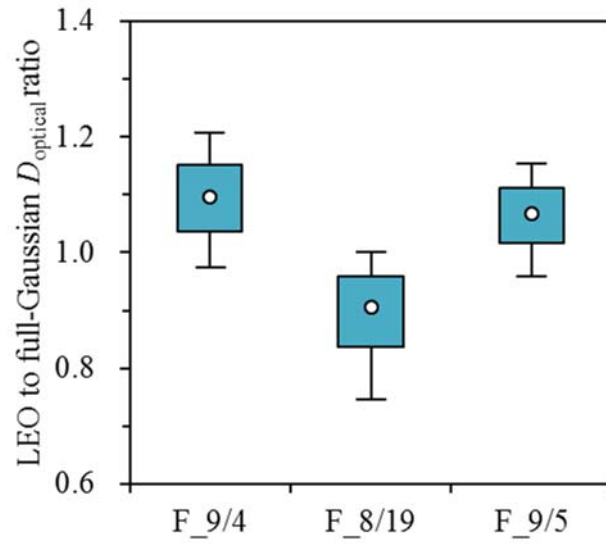
Figure 2. Relationships between optical sizes ($D_{optical}$) retrieved from the LEO and full-Gaussian fits for non-rBC containing particles observed during the three transformation flights conducted on September 4 (F_9/4), August 19 (F_8/19) and September 5 (F_9/5), 2013.
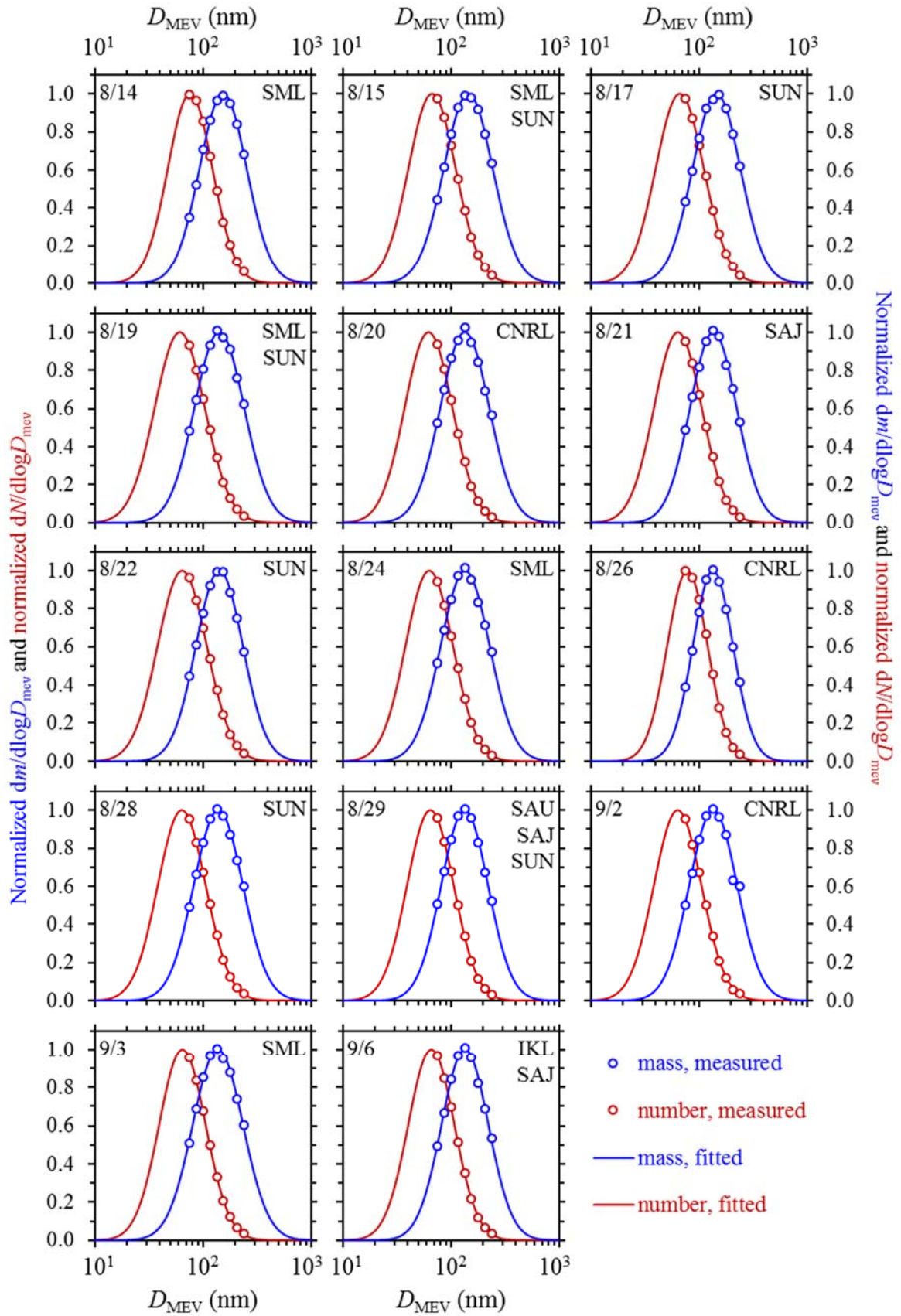
Figure 3. Mass and number size distributions of rBC for the 14 emission flights conducted over the OS facilities. For each flight, measured masses of individual rBC cores are first grouped into

different size bins and then fitted by a lognormal curve; rBC counts are processed similarly. Results from flight tracks between the airport and OS facilities are not involved in the analysis. Measurement date and the targeted OS facilities (1−3) are also shown for each flight. MMD, NMD, mass and number distribution widths, which are determined by lognormal fits to the measurement results, are summarized in Table S1 for these emission flights.
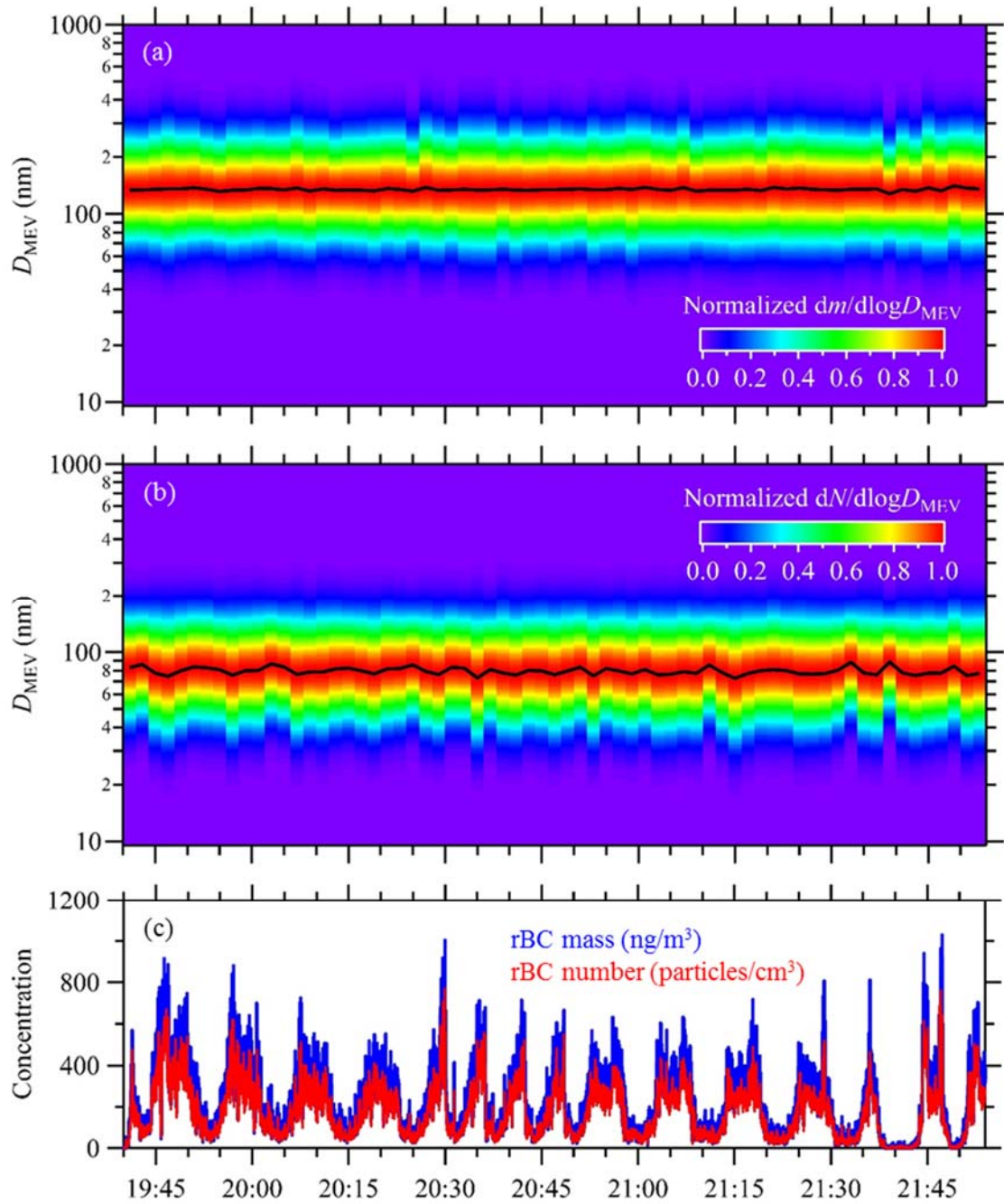
Figure 4. Time-resolved rBC **(a)** mass size distribution, **(b)** number size distribution, and **(c)** concentrations observed over the CNRL facility during F_8/26. Solid lines in (a) and (c) indicate MMD and NMD, respectively. The horizontal axis shows UTC time.
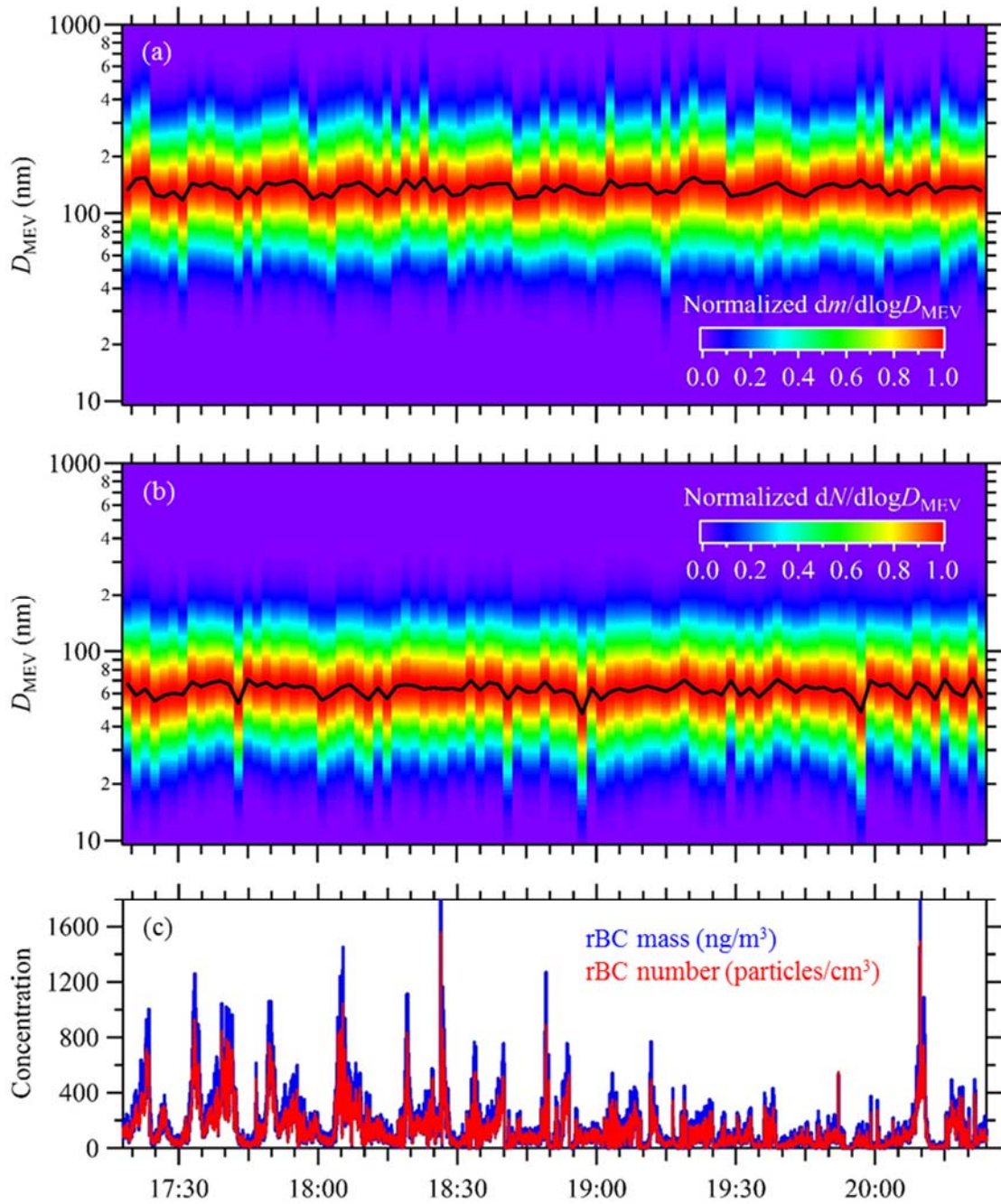
Figure 5. Time-resolved rBC **(a)** mass size distribution, **(b)** number size distribution, and **(c)** concentrations observed over the SUN facility during F_8/28. Solid lines in (a) and (c) indicate MMD and NMD, respectively. The horizontal axis shows UTC time. The flight track of F_8/28 is shown in Figure 1 (a).
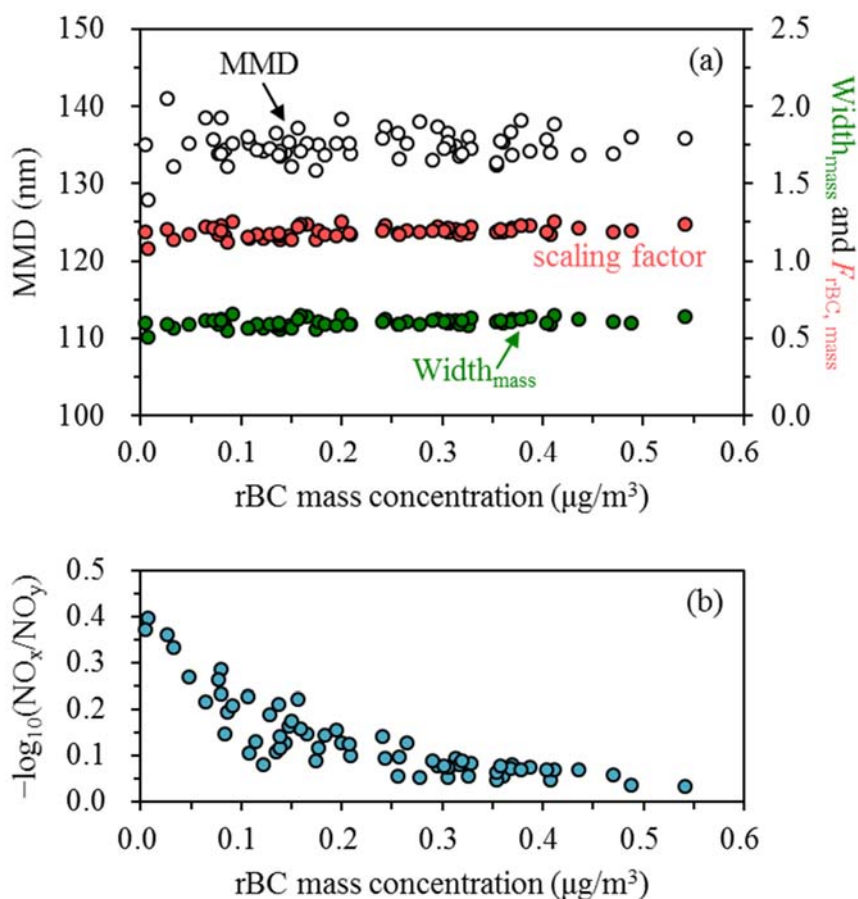
Figure 6. Dependences of **(a)** rBC MMD, mass distribution width (Width$_{mass}$), and mass-based scaling factor ($F_{rBC, mass}$), and **(b)** photochemical age on rBC concentration during F_8/26. Time resolution is 2 minutes for all the parameters shown here. Based on the temporal variation of 2-min averaged rBC mass concentration (Figure S3), rBC ≤ 0.1 μg/m³ can be used as an indicator for typical out-of-plume conditions during F_8/26. Uncertainties introduced by lognormal fitting are within ± 5 nm and ± 0.06 for the time-resolved MMD and Width$_{mass,}$ respectively.
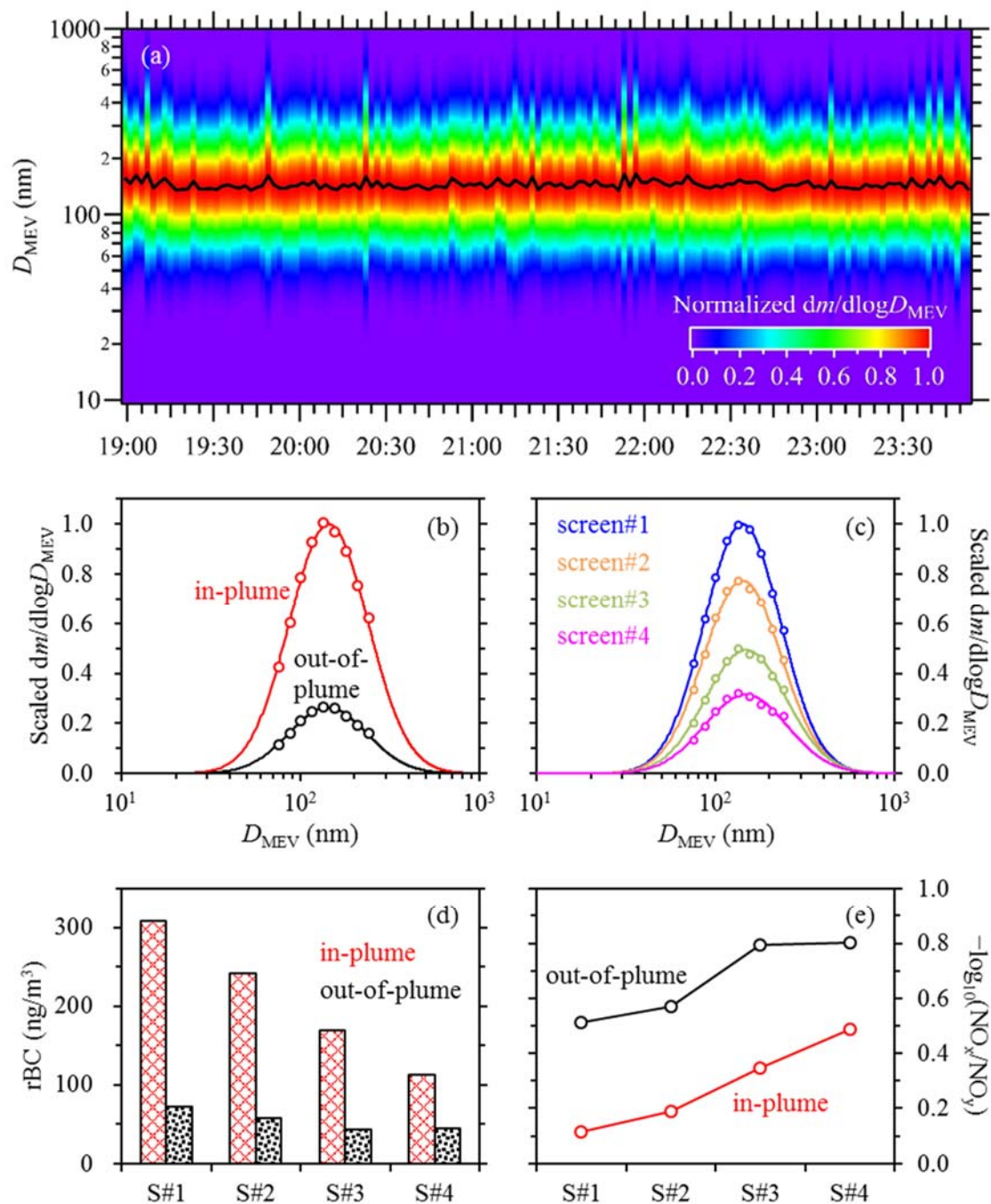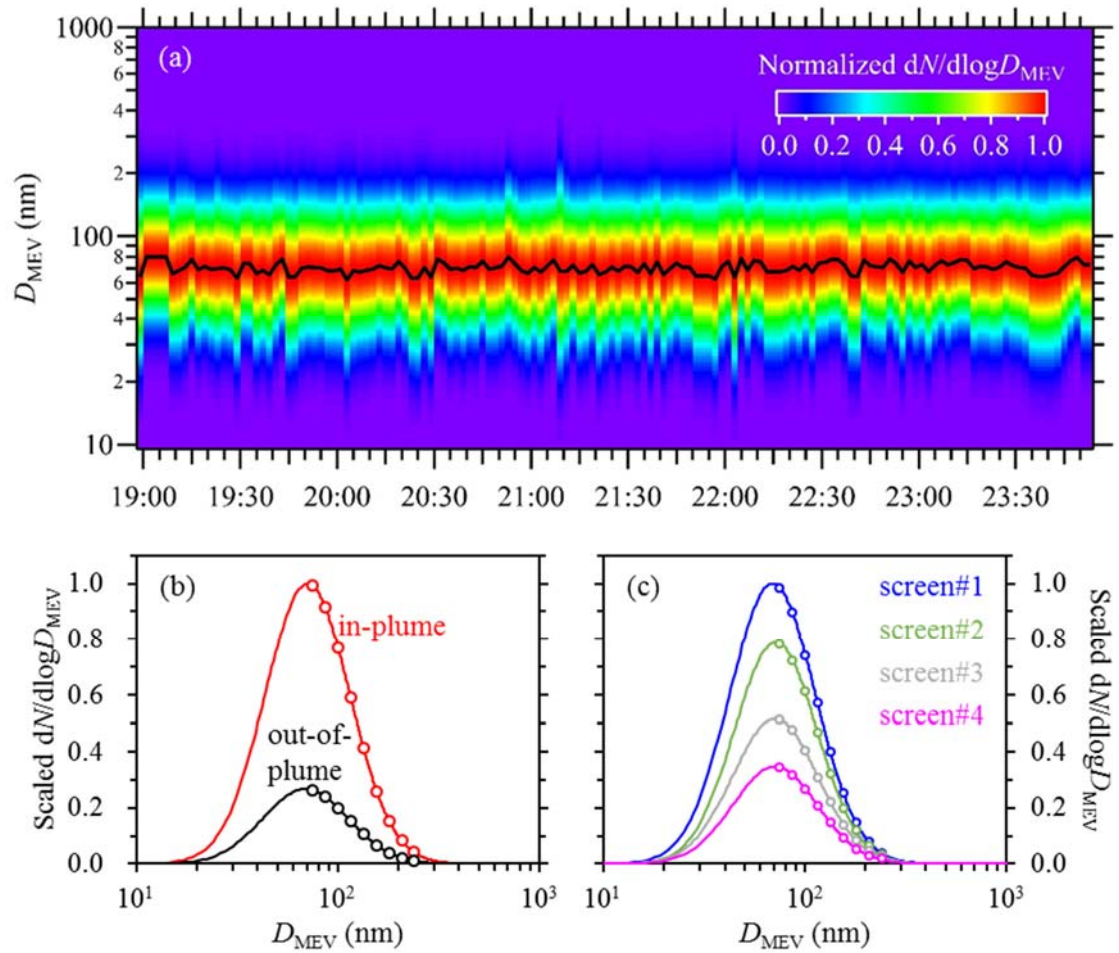
Figure 7. **(a)** Time-resolved rBC mass size distribution observed during the transformation flight F_9/4, **(b)** comparison of rBC mass size distributions between typical in- and out-of-plume conditions, **(c)** comparison of in-plume rBC mass size distributions among successive flight screens, and evolutions of **(d)** average rBC mass concentration and **(e)** photochemical age from screen #1 (S#1) to screen #4 (S#4). Scaling of out-of-plume rBC size distribution in (b), scaling of rBC size distributions for screens #2 to #4 in (c), and reason for excluding results from screen #5 in (c) to (e) are explained in the text.

Figure 8. (a) Time-resolved rBC number size distribution observed during the transformation flight F_9/4, **(b)** comparison of rBC number size distributions between typical in- and out-of-plume conditions, and **(c)** comparison of in-plume rBC number size distributions among successive flight screens. Scaling of out-of-plume rBC size distribution in (b) and scaling of rBC size distributions for screens #2 to #4 in (c) are explained in the text.
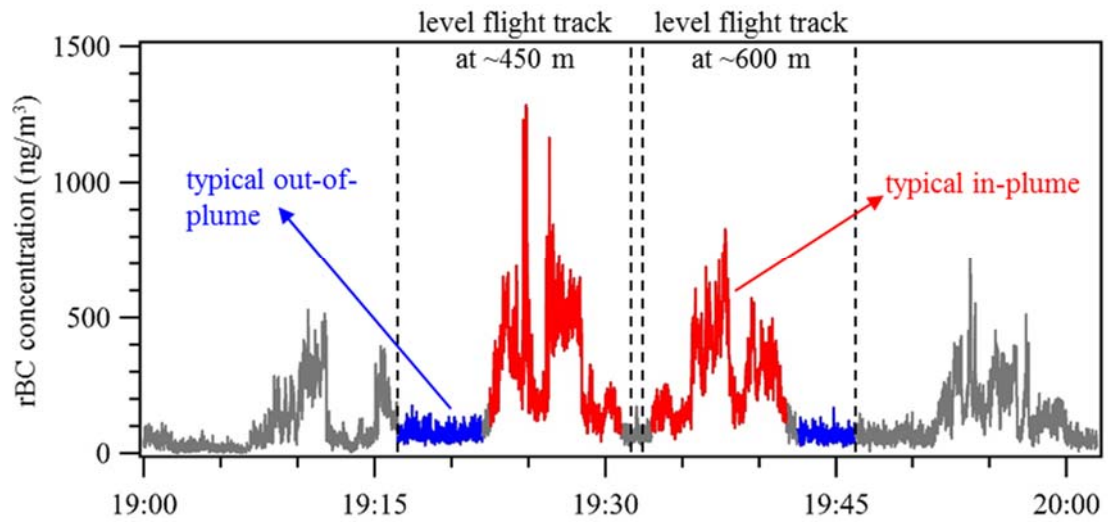
Figure 9. Identification of typical in- and out-of-plume conditions for two level flight tracks at ~ 450 and 600 m (in terms of ellipsoid height, equivalent to ~150 and 300 m above ground) on the first virtual screen of the transformation flight F_9/4.
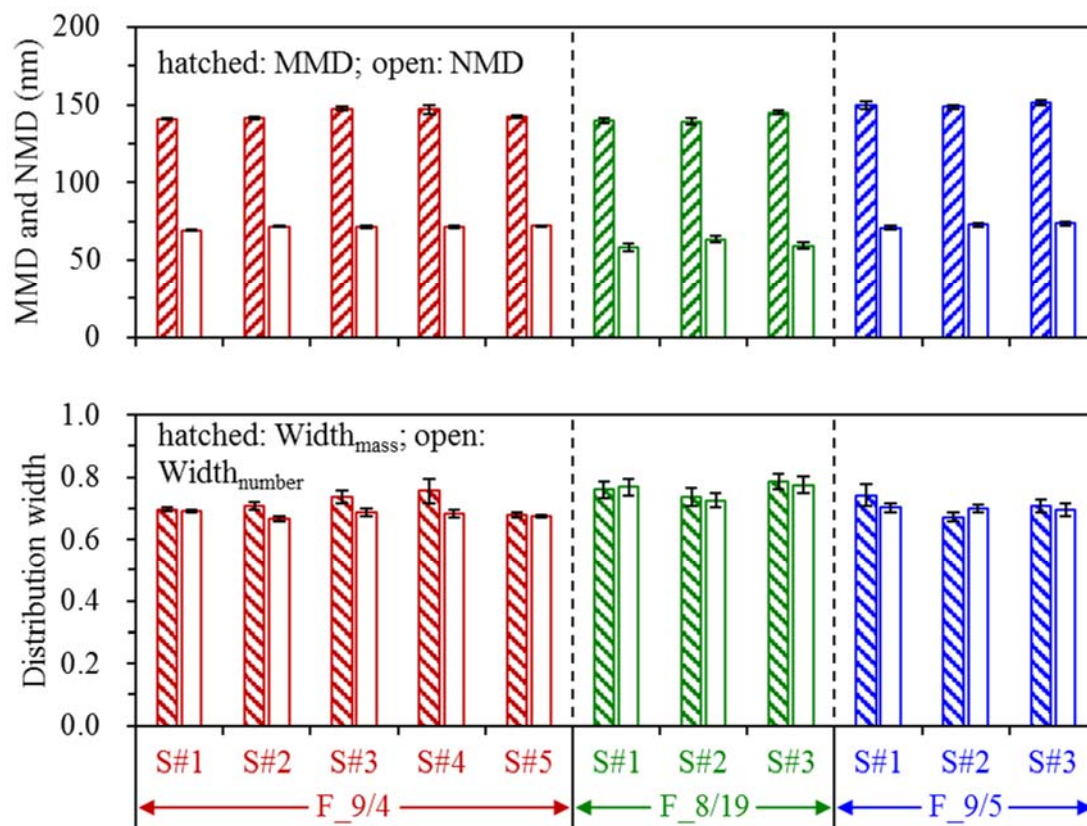
Figure 10. In-plume rBC MMD and NMD (upper pannel), and mass and number distribution widths (Width_mass and Width_number; lower panel) derived from successive flight screens of the three transformation flights. The results are also available in Table S2.
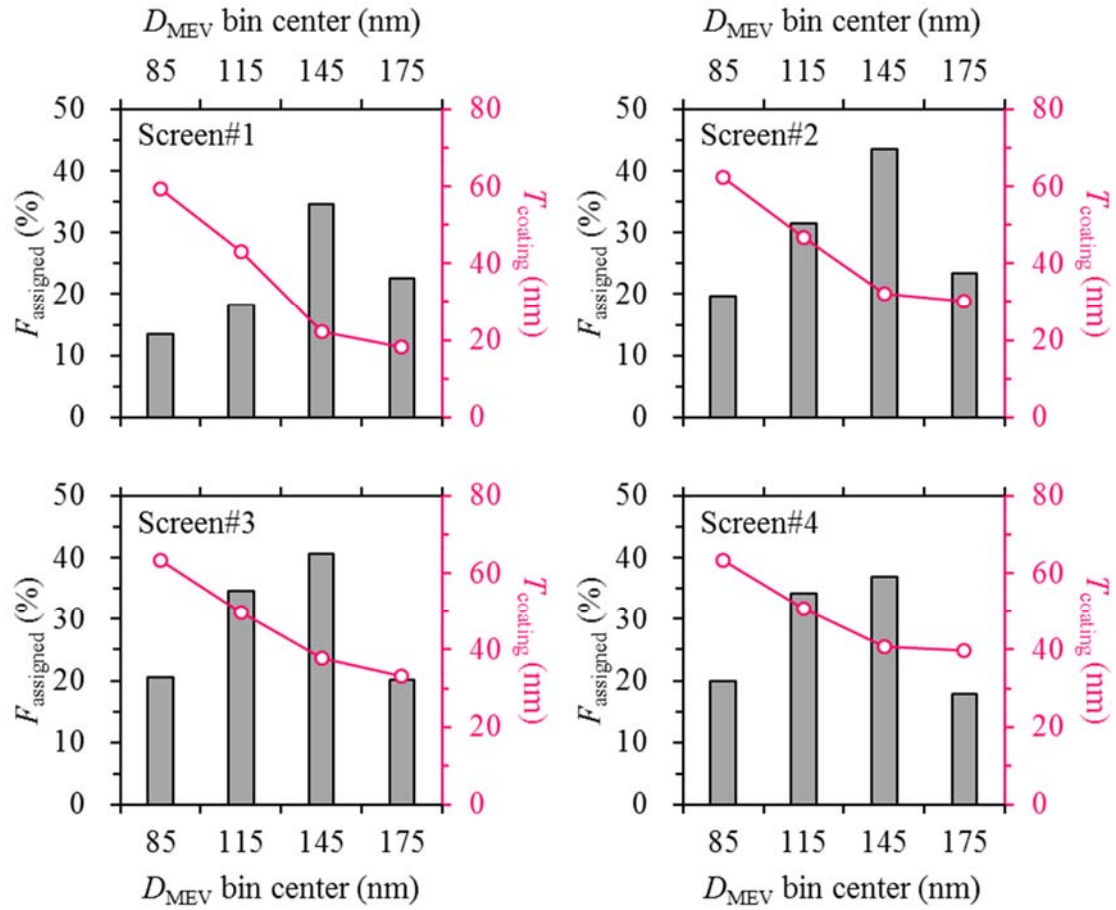
Figure 11. Dependence of coating thickness ($T_{coating}$) on rBC core size (D_{MEV}) for successive flight screens of the transformation flight F_9/4. To derive the dependence, rBC containing particles detected by the SP2 are divided into four equal-width bins according to their core sizes (D_{MEV}), the centers of which are 85, 115, 145, and 175 nm, respectively. The lower edge of the first D_{MEV} bin is 70 nm, corresponding to the SP2's lower detection limit of D_{MEV}; the upper edge of the last D_{MEV} bin is 190 nm. The D_{MEV} range of 70 to 190 nm accounts for approximately 95% of the detected rBC cores. For each D_{MEV} bin, the fraction of rBC cores that can be assigned a coating thickness ($F_{assigned}$, in %) is also shown.
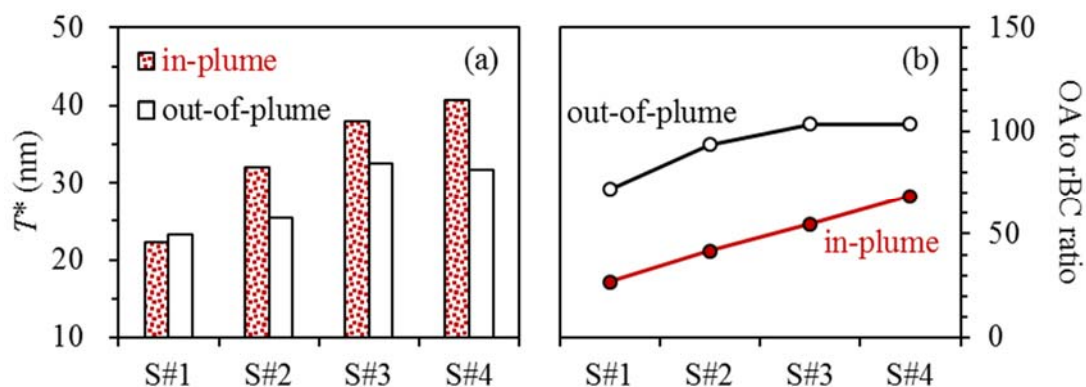
Figure 12. Evolutions of **(a)** coating thickness for rBC cores in the D_{MEV} range of 130−160 nm (T^*) and **(b)** OA to rBC mass ratio (OA/rBC) during the transformation flight F_9/4. Only median values are shown for T^* and OA/rBC. Quantitative discussions on OA/rBC have been presented elsewhere (Liggio et al., 2016), whereas statistical results are shown in Figure S5 for T^* measured during F_9/4 (together with T^* measured during the other two transformation flights). Evolution of coating thickness for rBC cores in the D_{MEV} range of 160−190 nm (Figure S6) exhibits the same pattern as that shown in (a). It should also be noted that the out-of-plume OA are dominated by pre-existing secondary organic aerosols formed from biogenic precursors (Liggio et al., 2016), which do not contribute to the formation of coating materials on rBC cores. This explains why the out-of-plume conditions have higher OA/rBC ratios but in general lower T^* compared to in plumes.